

Assessing Milankovitch forcing during and in the aftermath of the Early Eocene Climate Optimum: Dammam Formation, Saudi Arabia[☆]

Misbahu Abdullahi^a, Taimur Khan^a, Samer Aljurf^a, Vagif Suleymanov^b, Adhipa Herlambang^b, Michele Morsilli^c, Khalid Al-Ramadan^{a,b}, Ardiansyah Koeshidayatullah^{a,b,*}

^a Geosciences Department, College of Petroleum and Geosciences, King Fahd University of Petroleum and Minerals, Dhahran 31261, Saudi Arabia

^b Center for Integrated Petroleum Research, College of Petroleum and Geosciences, King Fahd University of Petroleum and Minerals, Dhahran 31261, Saudi Arabia

^c Dipartimento di Fisica e Scienze della Terra, Università di Ferrara, Via G. Saragat 1, 44100 Ferrara, Italy

ARTICLE INFO

Editor: L Angiolini

Keywords:

Milankovitch forcing
Cyclostratigraphy
Sedimentation Rate
Eocene
Dammam Formation
Early Eocene Climatic Optimum

ABSTRACT

The Eocene Epoch was a time of great climatic significance owing to its records of the Paleocene-Eocene Thermal Maximum (PETM), the Early Eocene Climate Optimum (EECO), and the Middle Eocene Climate Optimum (MECO). In the Arabian Plate, the EECO and its aftermath coincided with the development of the Lower to Middle Eocene Dammam Formation, a cyclic shallow-water carbonate ramp with meter-scale parasequences. Previous studies have shown the significance of Milankovitch forcing in pacing the Eocene events and deposition of sedimentary strata. However, the controlling process behind the high-resolution parasequences of the Dammam Formation remains enigmatic, particularly on the relative dominance between random and quasi-periodic Milankovitch forcing. To investigate this issue, we coupled continuous records of Spectral Gamma Ray (SGR), Magnetic Susceptibility (MS), and $\delta^{13}\text{C}$ - $\delta^{18}\text{O}$ data to assess the influence of astronomical forcing and the signature of how the Eocene climatic events are recorded in this formation. Results show that the overall low sedimentation rate recorded in the Dammam Formation is comparable with globally reported sedimentation rates of some shallow marine Eocene carbonates and compatible with low accommodation space on the Arabian carbonate ramp. Deposition was interpreted to be astronomically influenced based on the presence of eccentricity-paced parasequences, rejection of the null hypothesis ($p < 1\%$), and the detection of Milankovitch cycles. The EECO event is detected within the shales and *Alveolina-Nummulitic* intervals of the Midra and Alveolina Limestone members of the formation. This study provides the first assessment of Milankovitch forcing during and after the EECO marine records of the Arabian Plate, which could be compared elsewhere.

1. Introduction

The Eocene climate has received tremendous attention from both palaeoclimatologists and cyclostratigraphers owing to its record of long-term thermal events and Milankovitch-paced short-term hyperthermal events. These include the PETM (~56 Ma), the EECO (53.3–49.1 Ma), and their preceding or succeeding hyperthermals such as the Eocene Thermal Maximum (ETM) 2 & 3, I and J events (Kennett and Stott, 1991; Zachos et al., 1993; Zachos et al., 2001, 2008; Zeebe and Zachos, 2013; Lauretano et al., 2015, 2018), and the MECO (Barrera et al., 1993; Bohaty and Zachos, 2003; Cramwinckel et al., 2018; Giorgioni et al., 2019). Although the exact triggering mechanism for the events is still

debated, different hypotheses have been proposed to explain the source of the greenhouse gases responsible for the events, including decomposition of methane gas hydrates (Dickens et al., 1995), burning of peat and coal deposits (Kurtz et al., 2003), humid atmosphere (Bowen et al., 2004), etc. Outcomes of these events were an increased temperature (2–10 °C), a decrease in stable isotope ratios of carbon and oxygen, organic matter oxidation, elevated CO₂ and CH₄, and an increased sea level (Bowen et al., 2004; Lauretano et al., 2015), as well as some changes in carbonate factories (e.g., Morabito et al., 2024 and references therein). Due to the aforementioned peculiarities of Eocene events, the time interval provides a case study for investigating the impact of astronomical forcing on sedimentary strata (e.g., Westerhold and Röhl,

[☆] This article is part of a Special issue entitled: 'From rock to time' published in Palaeogeography, Palaeoclimatology, Palaeoecology.

* Corresponding author at: Geosciences Department, College of Petroleum and Geosciences, King Fahd University of Petroleum and Minerals, Dhahran 31261, Saudi Arabia.

E-mail address: a.koeshidayatullah@kfupm.edu.sa (A. Koeshidayatullah).

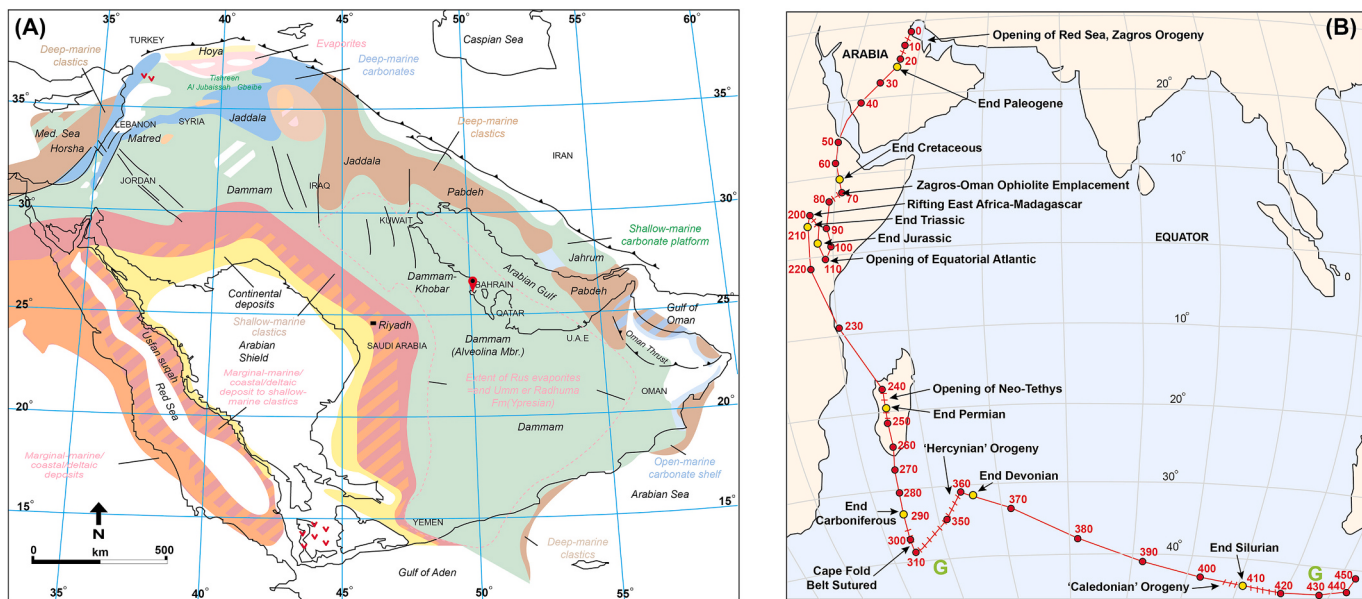


Fig. 1. (A) Paleo-facies map of the Eocene showing the deposition of Dammam Formation and its equivalents (After Ziegler, 2001). Note the location of the shallow well in red; (B) Map of the Arabian Plate showing changes in its geographical position over time (Al-Fares et al., 1998). The G's indicate timing of Paleozoic glaciations and the unit of red numbers are in Ma. (For interpretation of the references to color in this figure legend, the reader is referred to the web version of this article.)

2009; Wu et al., 2021; Messaoud et al., 2023; Brachert et al., 2023) and as an analog for understanding the response of the Earth system to current global warming (Zeebe and Zachos, 2013; Lauretano et al., 2015). Using $\delta^{13}\text{C}$ and $\delta^{18}\text{O}$ of benthic foraminifers in IODP sites 1262 and 1263, Lauretano et al. (2015) pinpoint that the short-lived hyperthermals were paced by 100 kyr and 405 kyr short and long eccentricity cycles, respectively. Other workers also showed dominance of eccentricity forcing on the Eocene Series (e.g., Huang and Hinnov, 2019; Messaoud et al., 2023; Brachert et al., 2023).

Cyclostratigraphy and its implications for palaeoclimate have been extensively studied across the stratigraphic record (e.g., Hinnov, 2018; Kodama and Hinnov, 2015; Wu et al., 2023). Most works utilized high resolution, continuous geochemical (e.g., $\delta^{13}\text{C}$, $\delta^{18}\text{O}$) and physical records (e.g., gamma ray, and magnetic susceptibility) in identifying the Milankovitch cycles and determining sedimentation rate, using various time-series analysis software packages (e.g., Paillard et al., 1996; Hammer et al., 2001).

Previous works on time series analysis of the Eocene are widespread in the literature (e.g., Huang and Hinnov, 2019; Wu et al., 2021; Messaoud et al., 2023, among others). However, no similar work has been conducted on the Arabian Plate for comparison to global events. Thus, we aim to (1) assess the influence of astronomical forcing on the Lower-Middle Eocene Dammam Formation in Saudi Arabia and determine the signature of how the Eocene climatic events are recorded in the formation using coupled continuous records of spectral gamma ray (SGR), magnetic susceptibility (MS), and whole rock stable isotope ratios ($\delta^{13}\text{C}$, $\delta^{18}\text{O}$) data performed on the carbonate fraction of the formation from a shallow well core; (2) determine the sedimentation rates and how they evolved throughout the deposition of the formation; and (3) determine the stratigraphic completeness of the formation in the study area. This pilot work thus provides insight into the effects of Milankovitch forcing during and after the EECO of the Arabian Plate that can be compared to other similar-aged strata globally.

2. Geological setting

The Dammam Formation covers the eastern shelf of the Arabian Plate (Fig. 1A) and represents the second '2nd-order' sequence AP10

that was associated with the maximum flooding surface (MFS Pg20) of Sharland et al. (2001). During deposition of the formation (i.e., Early-Middle Eocene), the Arabian plate was situated at a palaeolatitude of 10–20°N (Al-Fares et al., 1998; Fig. 1B). The formation is unconformably overlain by either the Miocene Hadrukh or Dam Formation, depending on location, and cover conformably the Rus Formation. The Dammam Formation is correlative across the plate, although some members are locally absent.

Based on biostratigraphic data, different ages have been suggested by previous workers. For example, Ziegler (2001) and Sharland et al. (2001) mentioned that the formation is regionally late Ypresian to Priabonian in age. In Saudi Arabia, Weijermars (1999) mentioned Ypresian (52 Ma) for the base and Lutetian (43.8 Ma) for the top of the formation (see also his Fig. 1)—implying a duration of 8.2 Myr. A similar age range was reported by Powers et al. (1966) in Saudi Arabia. These authors assigned the age of the two basal members (Midra & Siala Shales) based on three diagnostic large benthic foraminifera species—*Nummulites lucasana*, *Nummulites globulus*, and *Alveolina decipiens*, representing the late Ypresian period. They dated the Alveolina Limestone Member as early Lutetian based on the occurrence of *Linderina paronai*, *Dictyoconoides* sp., and *Alveolina elliptica*. The Khobar Member contains fossils indicative of early to middle Lutetian period, including *Nummulites somaliensis*, *Linderina buranensis*, and *Dictyoconoides cooki*, in addition to other additional diagnostic fossils. Al-Hashimi and Amer (1985) also mentioned the early to late Ypresian age for the lower part of the formation in Iraq. However, Al-Saad (2005 and references therein) assigned a middle-late Lutetian age for the formation in Qatar. Also worthy of mentioning is that exact numerical ages for the members of the formation are very limited in the literature.

In Saudi Arabia, the formation is divided into five members (from oldest to youngest): Midra Shale, Siala Shale, Alveolina Limestone, Khobar, and Alat Member (Powers et al., 1966). The Midra Shale, characterized by its yellow-brown color, consists of fissile, thinly laminated clay shale, grey marl, and soft limestone beds. Abundant shark teeth have led to its colloquial name, 'Shark Tooth' Shale (Powers et al., 1966). The Siala Shale differentiates itself from the Midra Shale by its brownish-yellow sub-fissile clay shale and contains, in addition to shark teeth, gastropods, fish spines, and indeterminate pelecypods. A 0.6 m

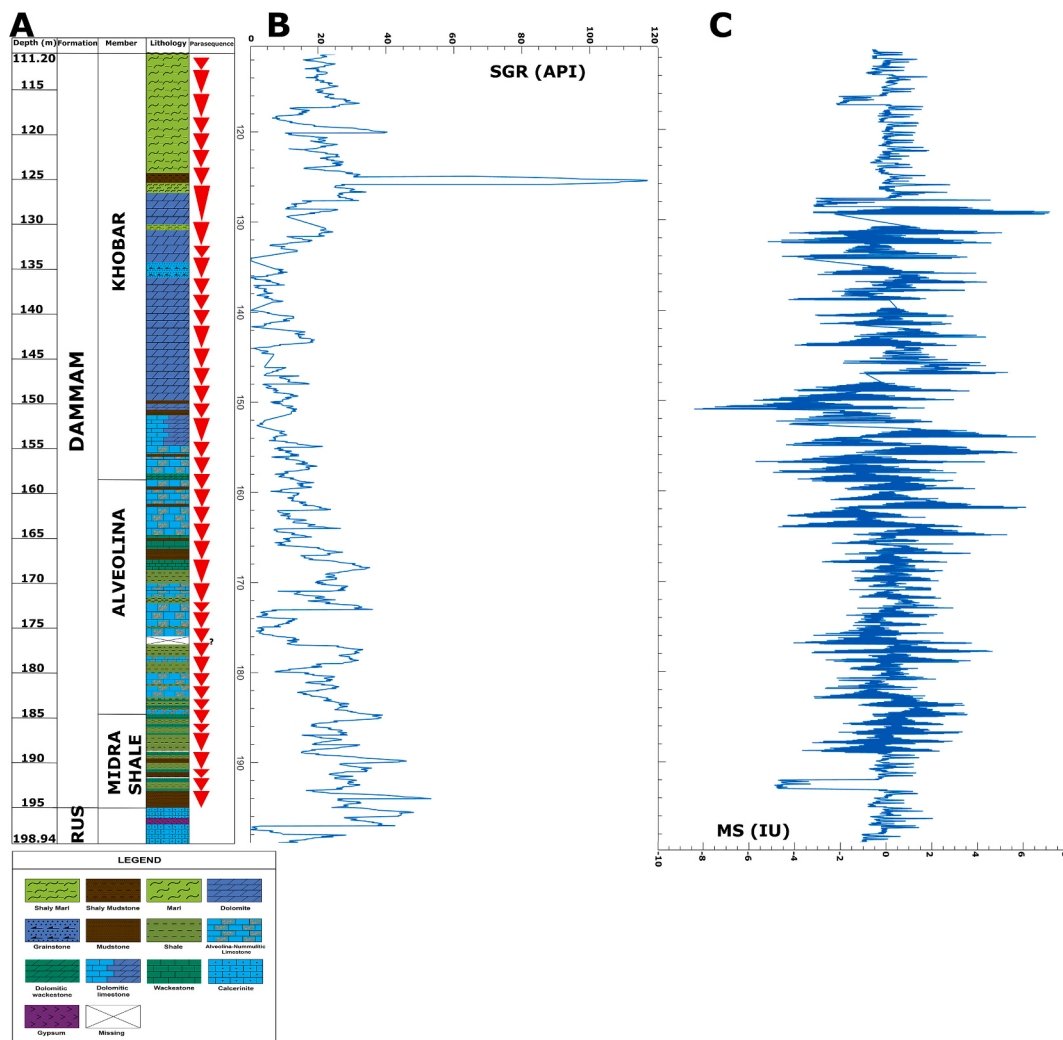


Fig. 2. (A) Core log of the studied section showing the Dammam Formation and some of its members in Saudi Arabia. The uppermost portion of the Rus Formation is also shown. The shoaling-upward parasequences are apparent and are shown using red triangles. (B) and (C) SGR and MS logs used as the proxy data in this study, plotted against stratigraphic depth (m). (For interpretation of the references to color in this figure legend, the reader is referred to the web version of this article.)

grey fossiliferous calcarenous limestone separates Saila from Midra (Weijermars, 1999), although Powers et al. (1966) consider it part of Saila Shale. The Alveolina Limestone Member is pale orange to yellow-grey, microcrystalline, recrystallized, and partly dolomitized limestone, with the presence of *Alveolina elliptica*, *Lucina pharaonic*, *Coskolina*, and *Nummulites* sp. The Khobar Member comprises units of Nummulites-bearing dolomitic limestone or dolomite, brown limestones (nummulitic and non-nummulitic), and marl. The Alat Member includes a basal unit of dolomitic marl overlain by light-colored porous and chalky dolomitic limestone plus marl and limestone (Powers et al., 1966; Tleel, 1973; Weijermars, 1999).

Eastern Arabia during the Eocene Epoch had relatively low accommodation (Sharland et al., 2001) punctuated frequently by local sea-level fluctuations. In this region, the Dammam Formation represents the terminal phase of an Eocene transgression, followed by retreat of the Tethyan Sea and regional exposure that resulted in the non-deposition of Upper Eocene and Oligocene sediments (Al-Saad, 2005). Lithological characteristics and faunal assemblages within the formation indicate cyclical deposition within a shallow, low-energy, warm, restricted-to-open-marine carbonate ramp (Weijermars, 1999; Al-Saad, 2005). Deposition of the Dammam Formation began with transgression, resulting in turbid open marine water covering the restricted marine environment of the Lower Eocene Rus Formation (Powers et al., 1966; Weijermars, 1999). This transgression led to the deposition of Saila and

Midra shales (Ziegler, 2001). With continued transgression, shale deposition gave way to clear-water Alveolina- and Nummulite-bearing carbonates before being terminated with the deposition of Neogene sediments due to Red Sea rifting accompanied by uplift of the Arabian Shield (Weijermars, 1999).

3. Data and method

Eighty-eight meters of shallow subsurface cores spanning the Lower-Middle Eocene Dammam Formation and a minor portion of the underlying Rus Formation (3.34 m; Fig. 2) were logged and then scanned using the MS3 Bartington Magnetic Susceptibility Meter to obtain Magnetic Susceptibility (MS) data. The core was gotten from a shallow well drilled at King Fahd University of Petroleum and Minerals (KFUPM) Beach, eastern Saudi Arabia ($26^{\circ}06'08.65''N$, $50^{\circ}06'53.94''E$; Fig. 1A) and stored at the College of Petroleum Engineering and Geosciences Core Analysis Laboratory (Room 2055). Spectral Gamma-ray (SGR) data was obtained from the College of Petroleum and Geosciences Learning Enrichment Centre Initiative team, which used a lab spectral gamma-ray core logger to scan the core at a vertical resolution of 5 cm. The SGR and MS values are reported in the API (American Petroleum Institute) unit and IU (Instrumental Units), respectively. To reduce errors in MS measurements, each meter of core was scanned twice at room temperature and atmospheric pressure, with resolutions dominantly ranging between

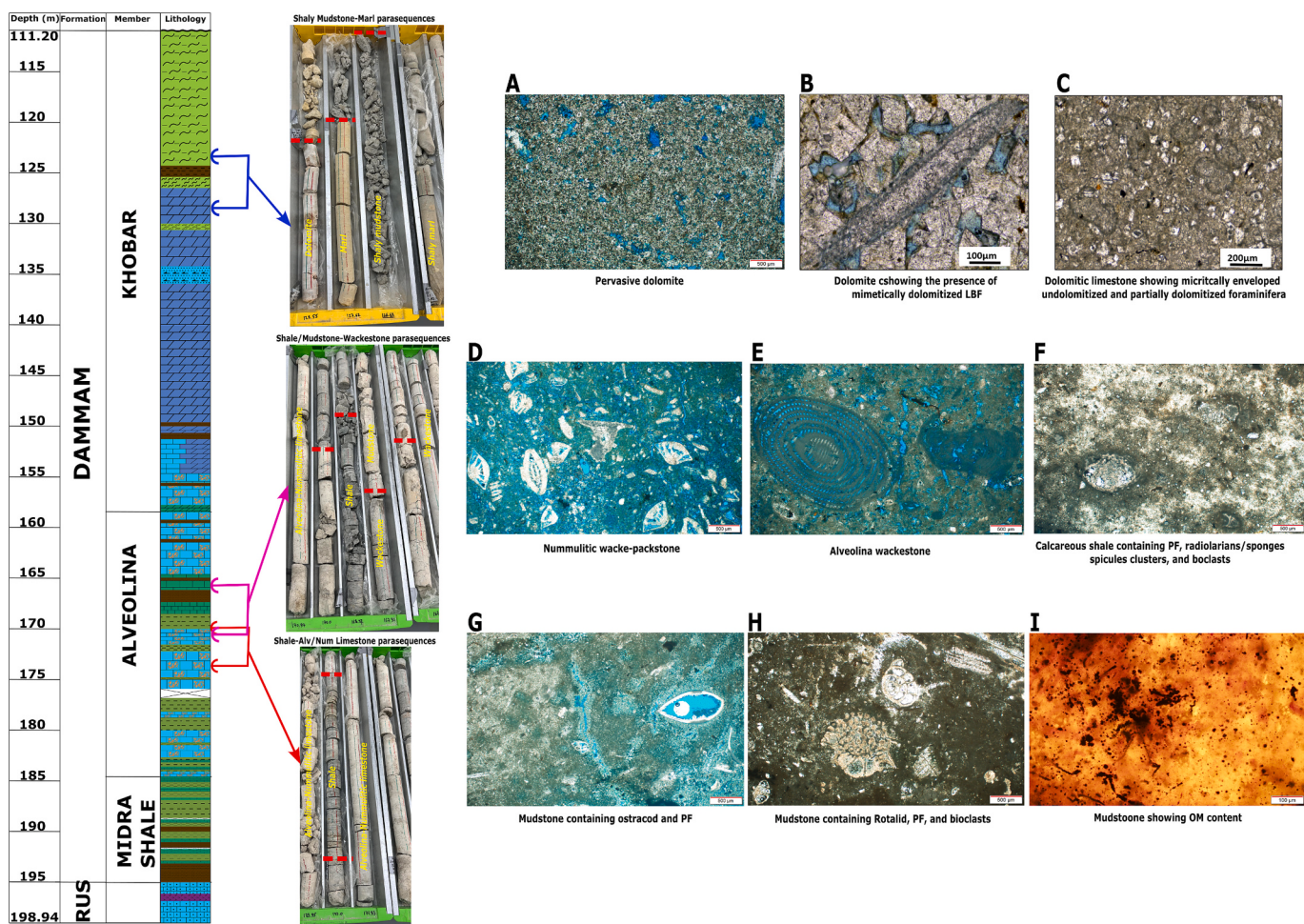


Fig. 3. Left Panel: Core log of the studied section. Middle Panel: Core photographs of some selected lithological cycles. The red dashed lines represent the boundaries between lithofacies. Right Panel: Thin section images of selected microfacies; (A-B) Dolomite, (C) Dolomitic foraminiferal wackestone, (D) Nummulitic wacke-packstone showing presence of rotaliids, (E) Alveolina wackestone, (F) Calcareous shale containing planktonic forams, radiolarians/sponge spicules clusters and bioclasts, (G) Mudstone containing ostracods and planktonic forams, (H) Mudstone containing rotalids, bioclasts, and planktonic forams, (I) Mudstone showing OM content. (For interpretation of the references to color in this figure legend, the reader is referred to the web version of this article.)

0.82 and 12.5 cm, and the data was averaged. A high-resolution whole rock carbon and oxygen stable isotope ratio ($\delta^{18}\text{O}$ & $\delta^{13}\text{C}$) measurement, with a sampling interval of 25 cm, was performed on the whole Dammam Formation. The samples were collected using a low-speed Dremel micro-drilling tool and analyzed on a Thermo Finnigan MAT-253 plus mass spectrometer, with an overall 1σ precision of 0.08 ‰ for $\delta^{18}\text{O}$ and 0.04 ‰ for $\delta^{13}\text{C}$ calculated on replicated actual samples. All values are reported relative to the Vienna Pee Dee Belemnite (VPDB) standard in parts per mil (‰). The stable isotope analysis was performed at the Stable Isotope Laboratory, King Fahd University of Petroleum and Minerals, Saudi Arabia.

For time series analysis, the software suite Acycle v2.4.1 (Li et al., 2019) was employed. The time series analysis was based on SGR and MS, each versus true vertical depth logs of the formations. Initially, the peak value at ~125 m of the SGR data was down-picked from 115.91 to a maximum of 50 API for a better amplitude uniformity with the rest of the data. Each of the data series (SGR & MS) was interpolated using its median value—0.050 m for SGR and 0.0116 m for MS—and then detrended using a 50 % rLOESS trend to remove long-term secular trends, have data fluctuate around a zero mean, and prevent spillover of power from very low-frequency elements into higher-frequency bands (Li et al., 2019).

We tracked the sedimentation rates (SAR) of the Dammam Formation using correlation coefficients from COCO and eCOCO using a

midpoint age of the formation (47.9 Ma) for the target astronomical solution (Li et al., 2018). COCO calculates the correlation between the power spectra of a geological proxy series in the depth domain and an astronomical model in the time domain (Li et al., 2018)—here, Eccentricity-Tilt-Precession (ETP) of La04 was utilized as the model (405 kyr long eccentricity, 125 and 95 kyr short eccentricity, 39.4 kyr obliquity, and 23.2, 21.9, and 18.8 kyr precession cycles; Laskar et al., 2004). This involves translating the proxy series from depth to time over various potential sedimentation rates using the Pearson correlation coefficient. The most probable sedimentation rate was identified by the highest correlation coefficient, lowest null hypothesis, and highest number of astronomical parameters. COCO also tests the null hypothesis (H_0) that there was no astronomical forcing, estimated using non-parametric Monte Carlo simulations. If the null hypothesis (H_0) significance level of the peak correlation coefficient recorded in the COCO is <1 %, then the null hypothesis of no astronomical forcing can be rejected (Li et al., 2018, 2019). In this work, Monte Carlo simulations of 2000 and a test sedimentation rate of 0–10 cm/kyr with a 0.01 cm/kyr window step were adapted for both the SGR and MS data series. Evolution of sedimentation rate through the series was done using eCOCO and a sliding window of 25 m, as it utilizes the full orbital frequency spectrum compared to eTimeOpt.

Based on the apparent vertical changes in SAR, the data series were segmented into three subsections (111.1–137 m, 137–176 m, and

176–198.94 m for the SGR and 111.1–137 m, 137–170 m, and 170–198.94 m for the MS). Each of these segments was pre-whitened using robust auto-regressive (AR1) autocorrelation and then detrended as explained above. The pre-whitening was performed to overcome potential bias of respective over- or under-estimation of high- or low-frequency cycles, which can be caused when the data is subjected to a robust AR1 red-noise model during spectral analysis (Weedon, 2022). Both MS and SGR data subsections were minimally tuned using a 100 kyr cycle to convert the depths to a floating age scale for the Dammam Formation. Before this tuning, a central frequency of 0.667 ± 0.02 cycle/m (1.5 m) was bandpass-filtered to represent the 100 kyr cycle for the bottommost segment of the two data series, 0.5 ± 0.002 cycle/m (2 m) for the middle segment of the two series, and 0.2 ± 0.03 cycle/m (5 m) and 0.25 ± 0.003 cycle/m (4 m) for the topmost segments of SGR and MS, respectively, using a Gaussian filter (Kodama and Hinnov, 2015). The filtering parameters were assigned based on the most representative SARs obtained from eCOCO of each segment.

Spectral analysis was performed on both the tuned and untuned data by employing the 2π multi-taper method (MTM) using a maximum frequency of 0.06 cycle/kyr and 10 cycle/m, respectively. A robust AR1 red-noise model was used to remove background noise (Mann and Lees, 1996). The tuned data series were interpolated using 2–4 kyr. Evolutive spectral analysis was finally performed to examine the persistence of the astronomical cycles using the Fast Fourier Transform (FFT) method with a sliding window of 12–15 m and 600–700 kyr for the untuned and tuned data, respectively.

4. Results

4.1. Core logging and description

The recorded thickness of the studied core is 84.7 m. Core logging (Fig. 2) shows the bottommost 3.34 m of the core is composed of two calcarenite units separated by a 0.5 m thick gypsum unit. These calcarenites are overlain by bioturbated, light-dark grey, yellowish-brown shales, mudstones and wackestones containing shark teeth, foraminifera, brachiopods, and ostracods. The fauna diversity and the bioturbation observed in this interval suggest an open marine setting and the high shale content may point to a turbid and low-energy condition with episodic terrigenous input. Cycles within this interval are underlain by fossiliferous shale or mudstone and capped by bioclastic wackestone (Fig. 2).

The previous interval changed to meter-scale cyclic mudstone/fissile shale-*Nummulitic/Alveolina* wacke-packstone parasequences considered to be shoaling-upward sequences based on organic-rich or calcareous shales (Figs. 2 & 3) typical of open marine at the base of most sequences (e.g., presence of planktonic foraminifera and radiolarians; Fig. 3) capped by *Alveolina-Nummulitic* wacke-packstones typical of mid-ramp setting (Fig. 3). The *Alveolina-Nummulitic* wacke-packstones exhibit chalky texture with first appearance at 185.72 m (Figs. 2 & 3). In some parasequences, *Nummulites/Alveolina* show a vertical decrease in size and abundance. Shallowing upward parasequences were identified in the core with thickness ranging between 1.05 and ~ 4.2 m. The capping wacke-packstones show changes vertically across the Alveolina Limestone Mbr. with dominant Alveolina content at the bottommost portion (e.g., Fig. 3E at ~ 183 m depth) and dominant Nummulite content as one goes up the parasequences (e.g., Fig. 3D at ~ 164 m depth). In some cases, the two are mixed in association with either rotaliids or miliolids. This association supports the interpretation that the capping Alv/Numm limestones represent a shallow marine environment in a ramp setting typical of the western Neo-Tethys Ocean (Martín-Martín et al., 2025). Generally, the large benthic foraminiferal content shows an increasing trend moving up the Alveolina Limestone Mbr—a trend that might be an indication of more favorable environmental conditions during the post-EECO event (e.g., Martín-Martín et al., 2025). This interval comprising the *Alveolina-Nummulitic* parasequences is generally interpreted to

Table 1

List of the identified facies and their brief description.

Microfacies	Description	Association
DF-1 and -2	Fossiliferous shale/mudstone and wackestone: contain foraminifera, brachiopods, ostracods, and/or fragments of shark teeth. It exhibits bioturbation and dominantly found within the Midra Mbr.	DF-3
DF-3	Foraminiferal mudstone: presence of planktonic foraminifera, sponge spicules cluster, radiolarians, and bioclasts. It usually contains organic matter	DF-4
DF-4	Fissile calcareous shale: shows clear fissility and presence of bioclasts similar to those observed in DF-3	DF-3
DF-5 and -6	Alveolina wackestone-packstone: contains dominantly of porcelaneous <i>Alveolinids</i> , biocalsts, and in cases minor unidentified miliolids; mostly observed at the lowermost half of Alveolina Mbr exhibiting a chalky texture.	DF-7 and – 8
DF-7 and -8	Nummulitic wackestone-packstone: dominantly contains of hyaline <i>Nummulitids</i> , biocalsts, and some rotaliids; mostly observed at the middle and upper half of Alveolina Mbr exhibiting a chalky texture.	DF-5 and – 6
DF-9	Alveolina-Nummulitic packstone: dominance of Nummulitids, with sporadic <i>Alveolinids</i> , <i>Rotaliids</i> and/or <i>Miliolids</i> ; observed at the uppermost half of Alveolina Mbr exhibiting similar chalky texture. DF-5 to -9 are difficult to differentiate by just mere looking at the core sample as they have similar coloration and texture.	DF-7 and – 8
DF-10 and -11	Dolomitic mudstone- wackestone: observed within the lowermost part of Khobar Mbr; presence of rhombic dolomite crystals of <50 mic mostly replacing the micrite; fossils are dominantly foraminifera	
DF-12	Dolomite: sucrosic euhedral rhombic dolomite that changes to an indurated subhedral-euhedral dolomite upward; dominantly pervasive and fabric destructive with few observable foraminifera and bivalves; presence of palygorskite and pyrite phases	DF-13, –14 and – 15
DF-13	Shaly mudstone: minor presence of <i>Alveolinids</i> , <i>Nummulites</i> , and <i>Operculina</i>	DF-12
DF-14	Bioclastic grainstone: well sorted, porous, dolomitic, and contains dominantly fragments of unidentified fossils that are in contact with one another	DF-12
DF-15	Marlstone-shaly marlstone: yellowish to brownish in color, shows some tiny iron concretion and generally indicates shalying upward to the top of the formation	DF-12

reflect a non-restricted or less-restricted mid-ramp setting due to the dominance of moderate to poorly bioturbated *Nummulitic-Alveolina*-rich packstone (Adabi et al., 2008; Banerjee et al., 2018).

A thick interval of grey to brownish sucrosic dolomite sits above these parasequences and is interbedded with thin units of shaly mudstones at the bottom and well-sorted porous grainstones, dolomite breccia, and marls at the top (Fig. 3). This dolomite-marl-dominated interval started at 158 m to the top of the core section. Some centimetre-thick missing intervals, related to recovery, are identified in the core (for example, at 190.06–189.93 m and 193–192.94 m; Fig. 2). The dolomite-marl-dominated interval is unconformably covered by sandy units which are likely of either the Miocene Dam or the Hadrukh Formation. This uppermost interval is interpreted to represent inner ramp shoal and back-shoal settings. This is because of the presence of *Alveolinids*, *Nummulites*, and *Operculina* in some of the beds, indicative of back-shoal facies, whereas the interbedded well-sorted porous grainstone could probably be representative of an inner ramp shoal with moderate to high energy conditions. Lack of bioturbation throughout the interval could signpost a restricted condition, although the

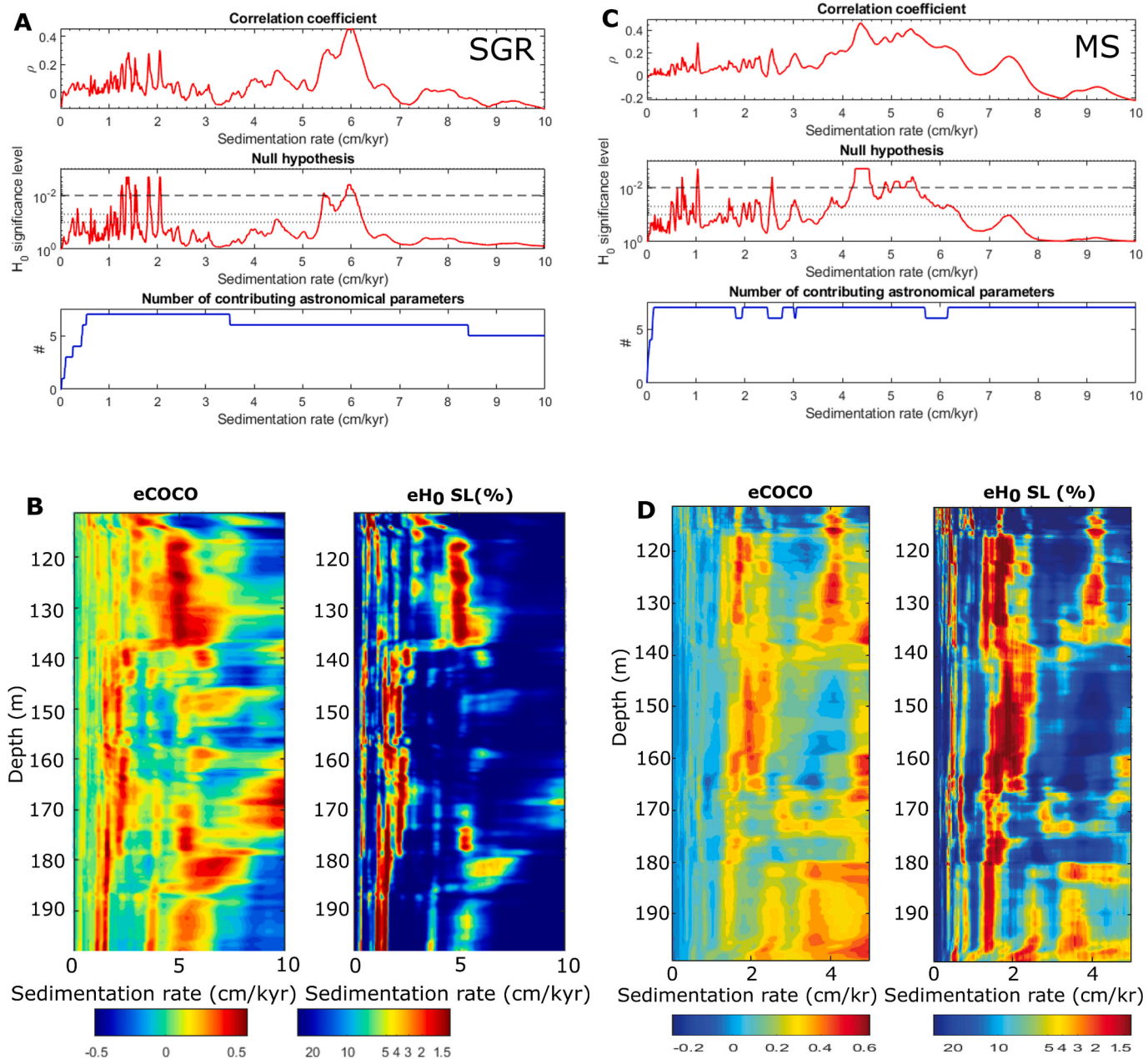


Fig. 4. Respective COCO and eCOCO plots of the two series (A and B) SGR, (C and D) MS. Each series was tested at a sedimentation rate range of 0 to 10 cm/kyr, a time step of 0.01 cm/kyr and Monte Carlo simulations of 2000. The target astronomical solutions are from the La2004 solution (Laskar et al., 2004) at the middle age of Dammam Formation (47.9 Ma).

bioturbation may be masked by the pervasive dolomitization. The presence of palygorskite clay in the dolomite samples may further support the restricted condition of this interval (Weaver and Beck, 1977; Chen et al., 2004; Xie et al., 2013), although this clay is likely secondary. Table 1 summarizes all the identified facies based on core logging and thin section observations.

4.2. Sedimentation rate

Correlation Coefficient (COCO) analysis shows sedimentation rates ranging from 1.28 to 2.06 cm/kyr and between 5.5 and 6 cm/kyr for the SGR (Fig. 4A). Meanwhile, the COCO of the MS data shows 1.06, 2.5, and between 4.4 and 5.4 (Fig. 4C) cm/kyr. Most of these SARs satisfy the conditions of the correlation coefficient (ρ), null hypothesis (H_0), and astronomical parameters (Li et al., 2018).

Evolutive COCO (eCOCO) shows that for the SGR data series, sedimentation rate evolved from a stable rate of ~1.5 cm/kyr from the bottom of the series until 176 m, which then increased to ~2 cm/kyr at ca. 176–137 m, and then abruptly increased to as high as ~5 cm/kyr at the topmost part of the formation (Fig. 4B). The eCOCO results for MS show similar stable SAR from the bottom to ca. 170 m but increased to ~2 cm/kyr between 170 and 137 m before finally increasing to ~4 cm/kyr to the top of the series (Fig. 4D). Although the two datasets show some dissimilarities in terms of their COCO and eCOCO, the results are overall comparable. Based on the vertical SAR variation from the two series, the following SARs are selected as the optimal rates for the three segments mentioned above: 1.5 cm/kyr (bottom-176/170 m), 2 cm/kyr (176/170 m to 137 m), and 5 or 4 cm/kyr (137 m to the top for SGR or MS, respectively). This means that ~6 m, ~1.88 m, 1.5 m, 0.6 m, and 0.3 m stratigraphic cycles likely represent ~405 kyr, 125 kyr, 100 kyr,

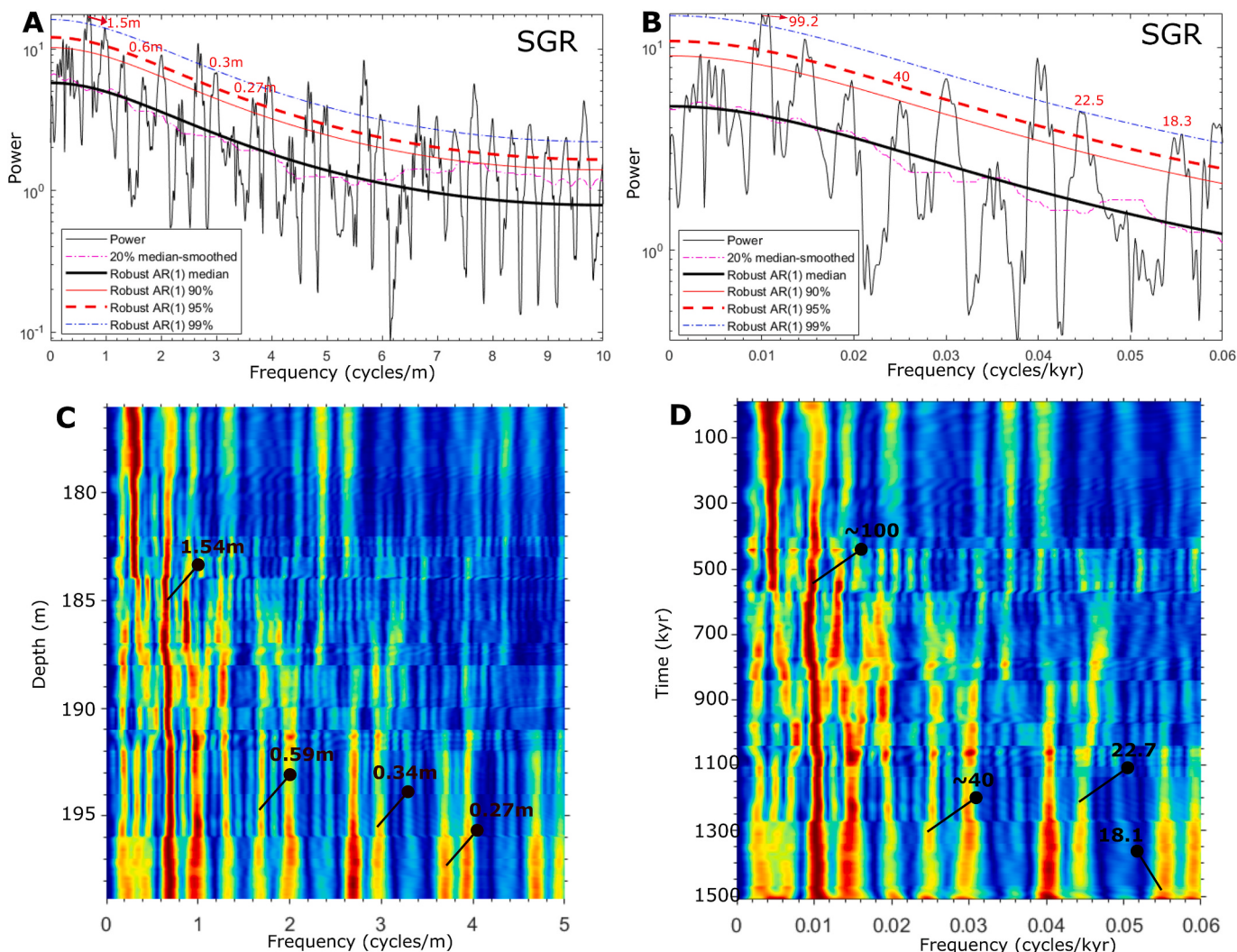


Fig. 5. Spectra and evolutive spectra of the bottom segment of untuned (A–B) and 100-kyr tuned (C–D) SGR series. Significant peaks corresponding to Milankovitch cycles are shown.

40 kyr, and 20 kyr astronomical cycles for the bottommost segment. Furthermore, it suggests that ~8 m, 2.5 m, 2 m, 0.8 m, and 0.4 m represent similar astronomical cycles for the middle segment of the two series. In the same line, 20 m, 6.25 m, 5 m, 2 m, 1 m cycles and 16 m, 5 m, 4 m, 1.6 m, 0.8 m cycles will represent similar astronomical cycles for the topmost segments of SGR and MS, respectively.

4.3. Cyclostratigraphy

The bottommost segment (i.e., bottom to 176 m) of the SGR series exhibits significant peaks at 1.5 m, 0.6 m, 0.3 m, and 0.27 m on the untuned power spectrum. Mirror images of these values are also apparent on the tuned spectrum of this segment with peaks at 99.2 kyr, 40 kyr, 22.5 kyr, and 18.3 kyr, respectively (Figs. 5A & B). Meanwhile, both the untuned (and tuned) spectra of the bottommost segment of the MS series show peaks at 1.92 m (127.2 kyr), 1.41 m (~94 kyr), 0.63 m (43.2 kyr), 0.34 m (22.8 kyr), 0.29 m (20.1–19.9 kyr), and 18.2 kyr (Figs. 6A & B). On the other hand, the SGR middle segment (i.e., from 176 m to 137 m) shows peaks at 2.47 m, 1.99 m, 0.43 m, and 0.4–0.38 m on its spectrum, which corresponds nearly to the 125.8 kyr, 94.3 kyr, 22.4 kyr, and 20.1–19.9 kyr peaks on its tuned spectrum, respectively (Figs. 7A & B). Meanwhile, the same segment (170 m to 137 m) exhibits peaks at 2.43 m, 1.99 m, and 0.41–0.39 m on the MS untuned spectra, corresponding nearly to the 121.2 kyr, 99.3 kyr, and 20–19.6 kyr

recorded on its tuned spectra (Figs. 8A & B). The top spectra of the two data series show the following peaks: 7.62–4.98 m, 2.09 m (SGR untuned), and 102.9 kyr, 43.3 kyr (SGR tuned); 4.46 m, 1.62 m, 0.71 m (untuned MS), and 100.7 kyr, 44.4 kyr, 17.9 kyr (tuned MS) (Figs. 9A & B; 10 A & B). Thus, 100 kyr short-eccentricity cycles were filtered from each of the series using the band-pass filter parameters mentioned above. The results yielded 15, ~20, and 5 short-eccentricity cycles for the respective bottommost, middle, and topmost segments of the SGR series, while ~19, 16, and 6 cycles are yielded for similar segments of the MS series, suggesting a duration of ~4–4.1 Myr for the whole studied core (Fig. 11).

Comparing the significant peaks of the SGR and MS stratigraphic power spectra and the target astronomical solution spectra of La2004 (Laskar et al., 2004) for the middle age of the Dammam Formation (~52 to ~43.8 Ma = ~47.9 Ma) indicates a reasonable match of the considered astronomical parameters (125 and 95 kyr short eccentricity, 39.4 kyr obliquity, and 23.2, 21.9, and 18.8 kyr precession cycles; Laskar et al., 2004) in most of the cases, albeit in some cases the parameters either shift to higher or lower frequencies or exhibit low power (Figs. 5–10). The evolutive FFT plots of the segmented series show that the lower frequency cycles (e.g., ~100 kyr short eccentricity) are more consistent than the higher frequency cycles (e.g., 20 kyr precession) (Figs. 5C & D to 10C & D). However, as expected, MS evolutive spectra show better consistency and higher power of the higher frequency cycles

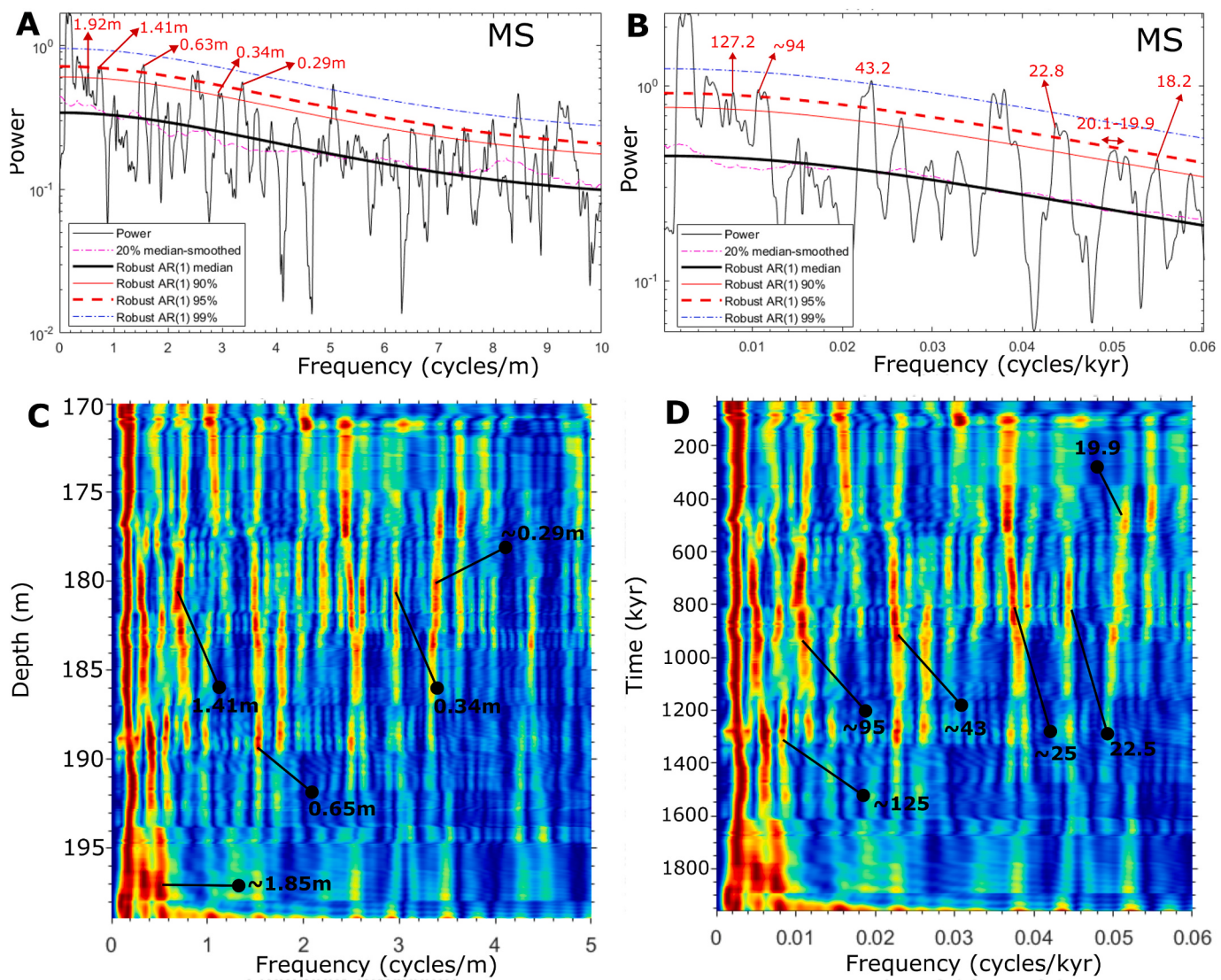


Fig. 6. Spectra and evolutive spectra of the bottom segment of untuned (A–B) and 100-kyr tuned (C–D) MS series.

in most of the plots, which is likely due to its higher resolution.

4.4. Stable isotopes

$\delta^{13}\text{C}$ and $\delta^{18}\text{O}$ signals show respective apparent excursions at depths of ~ 187 m (-3.9% and -8.8%), 177 m (-2.75% and -8.6%), and 168 m (-2.25% and -7.7%) (Fig. 11). Minor excursions are also observable at depths of 194 m (-2.23% and -4%) and ~ 156 m (0.7% and -5.3%). After the minor excursion at ~ 156 m, $\delta^{13}\text{C}$ continues with a narrow range of $+1$ to $+1.8\%$ until a depth of ~ 133 m, where it shows an abrupt shift to a negative value that generally continued to deplete until the top of the formation. Meanwhile, the $\delta^{18}\text{O}$ shows a general enrichment trend to the top of the formation, although a narrow range of between -0.6 and $+0.2\%$ is observed from a depth of 144 to 133 m. Overall, the whole rock $\delta^{18}\text{O}$ curve shows a general increase from the lower section of the formation to the upper section (Fig. 11). Additionally, there is a shift of $+2$ to $+4\%$ between the $\delta^{18}\text{O}$ of calcite and dolomite (Figs. 11 & 12B). The highest recorded value of $\delta^{13}\text{C}$ is $+2.7\%$, and the lowest is -3.9% , while the highest for $\delta^{18}\text{O}$ is $+2.2\%$, and the lowest $\delta^{18}\text{O}$ is -8.8% .

5. Discussion

5.1. Relationship between the physical proxies (SGR & MS) and the lithology

Our magnetic susceptibility (MS) and spectral gamma ray (SGR) records show a clear lithological control. Pure limestone intervals yield consistently low MS values, paralleled by low SGR responses (e.g., the Alveolina Member; Figs. 2–3). By contrast, marly-dominated intervals enriched in detrital material display markedly higher MS and SGR values. This parallel increase supports the interpretation of enhanced terrigenous influx during intervals of lowered sea level (Fig. 2). Moreover, many of the identified cycles exhibit a systematic coupling: higher MS–SGR values at the cycle bases and lower values toward the tops, reflecting stratigraphically consistent variations in clay content and radioactive mineral concentration.

These trends can be understood in the broader geophysical and geochemical framework. Gamma-ray responses primarily reflect the radioactive element content of rocks and sediments (Wahl, 1983). Spectral gamma ray (SGR) measurements quantify uranium, thorium, and potassium (Hassan et al., 1976), which are widely used to differentiate lithologies and reconstruct climatic variations (Peng et al., 2024 and references therein). Carbonates typically display low gamma-ray

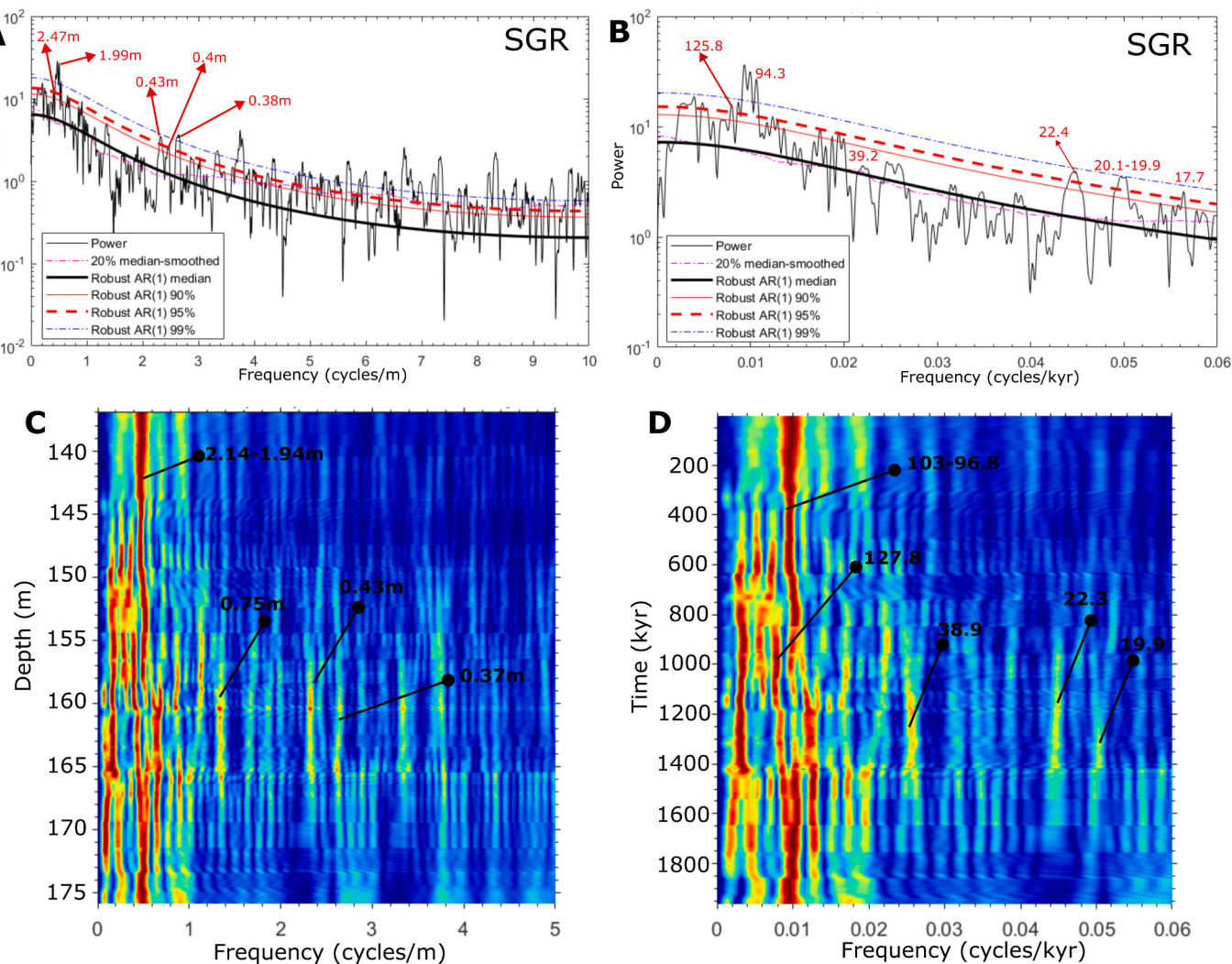


Fig. 7. Spectra and evolutive spectra of the middle segment of untuned (A-B) and 100-kyr tuned (C—D) SGR series.

values compared to siliciclastics due to their reduced concentrations of radioactive elements (e.g., Asquith and Krygowski, 2004). Conversely, organic-rich shales and mudstones are enriched in radioactive elements, yielding higher gamma-ray values than organic-lean equivalents.

Magnetic susceptibility reflects the concentration of magnetizable minerals in a rock (Ellwood et al., 2000). These include paramagnetic phases such as clays, ferromagnesian silicates, and Fe-sulfides, as well as ferrimagnetic minerals like magnetite; in carbonates, paramagnetic minerals generally dominate the signal. Increased detrital input proportionally enhances MS values, whereas pure calcite shows very low responses (Ellwood et al., 1999, 2000). Consequently, high-frequency MS variations capture subtle lithological changes linked to climatically driven fluctuations in terrigenous supply (Boulila et al., 2008).

5.2. Sedimentation rate

Results from the eCOCO analysis have shown that the Dammam Formation exhibits SARs ranging from ~1.5 to 5 cm/kyr, with the majority of the studied units having SARs of between 1 and 2 cm/kyr (Fig. 4). Rates comparable to the eCOCO estimation of Dammam Formation have been reported for Middle Eocene shallow marine carbonates of Neo-Tethys in Tunisia (2.86 cm/kyr, Messaoud et al., 2023). The low sedimentation rate of the Dammam Formation is consistent with its deposition on a broad carbonate ramp, where limited accommodation is expressed by the reduced thickness of this stratigraphic unit.

The Dammam Formation is identified as the second ‘2nd order’ sequence within the AP10 megasequence (Sharland et al., 2001). The Midra shale member represents the TST with a consistently low sedimentation rate at the bottom of the Dammam Formation (the interval was picked from the bottom of the formation that is dominated by fissile, grey to yellowish-brown shales to the first appearance of the *Alveolina-Nummulitic* limestone at 185.72 m). This indicates settling of fine sediments during Ypresian to early Lutetian, with turbid marine conditions associated to the beginning of the transgressive phase over the Arabian plate (Powers et al., 1966; Weijermars, 1999; Sharland et al., 2001; Ziegler, 2001). The interval between 170 m and 140 m shows a relatively higher sedimentation rate (2.0–2.3 cm/kyr), corresponding to the thick cyclic *Alveolina-Nummulitic* wacke-packstones and dolomite intervals of the *Alveolina* Limestone (picked from the first appearance of the *Alveolina-Nummulitic* limestone to the first occurrence of dolomitic/recrystallized limestone at 158 m) and Khobar members, respectively (Figs. 2 & 4). This interval is most likely indicative of a favorable carbonate factory production under relatively clear water conditions. The highest SAR (4–5 cm/kyr) is recorded at the topmost interval of the studied formation, which is dominated by marly units. The increased SAR at this interval could be due to the increased detrital flux compared to the lower intervals.

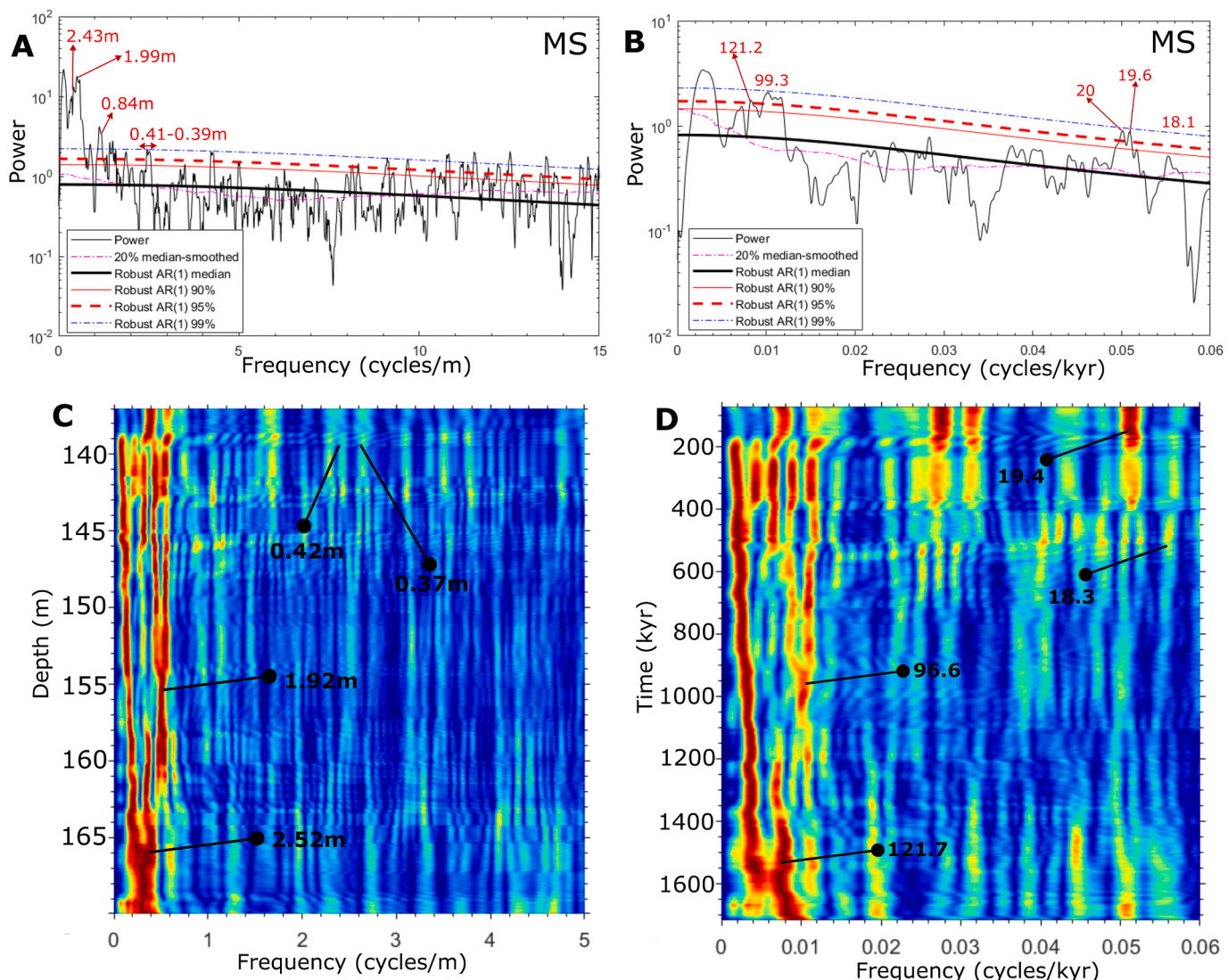


Fig. 8. Spectra and evolutive spectra of the middle segment of untuned (A–B) and 100-kyr tuned (C–D) MS series.

5.3. Potential diagenetic impact on palaeoclimate proxies

Although it can be argued that the observed stable isotope signals might be altered and not representative of the original marine signals, an argument can be made for less alteration of these signals for the Midra to Alveolina Limestone Member interval. These arguments are:

- (1) The predominant bio-components of the Alveolina Limestone and Midra shales are larger and smaller benthic foraminifera and brachiopods (Fig. 3) originally composing mainly of low magnesium calcite (LMC) and high magnesium calcite (HMC) mineral phases that are more resistive compared to aragonite, albeit HMC to LMC stabilization can still happen, especially in the alveolinids (Budd and Hiatt, 1993).
- (2) The +2 to +4 ‰ shift between the $\delta^{18}\text{O}$ of calcite and dolomite intervals is closer to the fractionation expected of co-genetic, co-existing marine calcite and dolomite (Tarutani et al., 1969; Land, 1980; Figs. 11 & 12B), which supports little meteoric interference. Again, no correlation was observed between the whole rock $\delta^{13}\text{C}$ and $\delta^{18}\text{O}$ of both the whole core interval and the proposed EECO interval, i.e., ca. 170 m to the bottom of the Dammam Formation (Fig. 12A). Negligible to weak correlations are also apparent when the stable isotopes are plotted based on lithofacies

(Fig. 12B). Interestingly, the majority of the lithofacies exhibit isotope clustering that could suggest variations in fractionations (e.g., vital effect) during the deposition of the facies, or if any, during early mineralogical stabilization (Fig. 12B). If we assume an Eocene $\delta^{18}\text{O}_{\text{SMOW}}$ of $\sim -1 \text{ ‰}$ (Zachos et al., 1994), an Eocene seawater surface temperature of 25–36 °C (Zachos et al., 2006; Pearson et al., 2007; Evans et al., 2018), and roughly use the fractionation equation of Kim and O’Neil (1997), calcite that formed from an Eocene seawater should have $\delta^{18}\text{O}$ of between -3.3 and -5.3 ‰ . Alveolina-Nummulitic limestones and other facies (e.g., some bioclastic wackestones and calcareous shales) show $\delta^{18}\text{O}$ values typical of the estimated Eocene calcite, further supporting the little diagenetic alterations of these facies (Fig. 12B). The marly facies that show higher values could represent facies deposited from colder seawater than those assumed above. The studied core intervals are interpreted by Abdullahi et al. (2025) to represent open marine, subtidal to non-restricted lagoonal environments (see also Weijermars, 1999), and the same study shows little meteoric influence on the diagenesis of the Dammam Formation (although focused mainly on the dolomite section).

- (3) The drill core samples are shallow ($<200 \text{ m}$), and the tectonic history from the Eocene to the present is dominated by uplift due

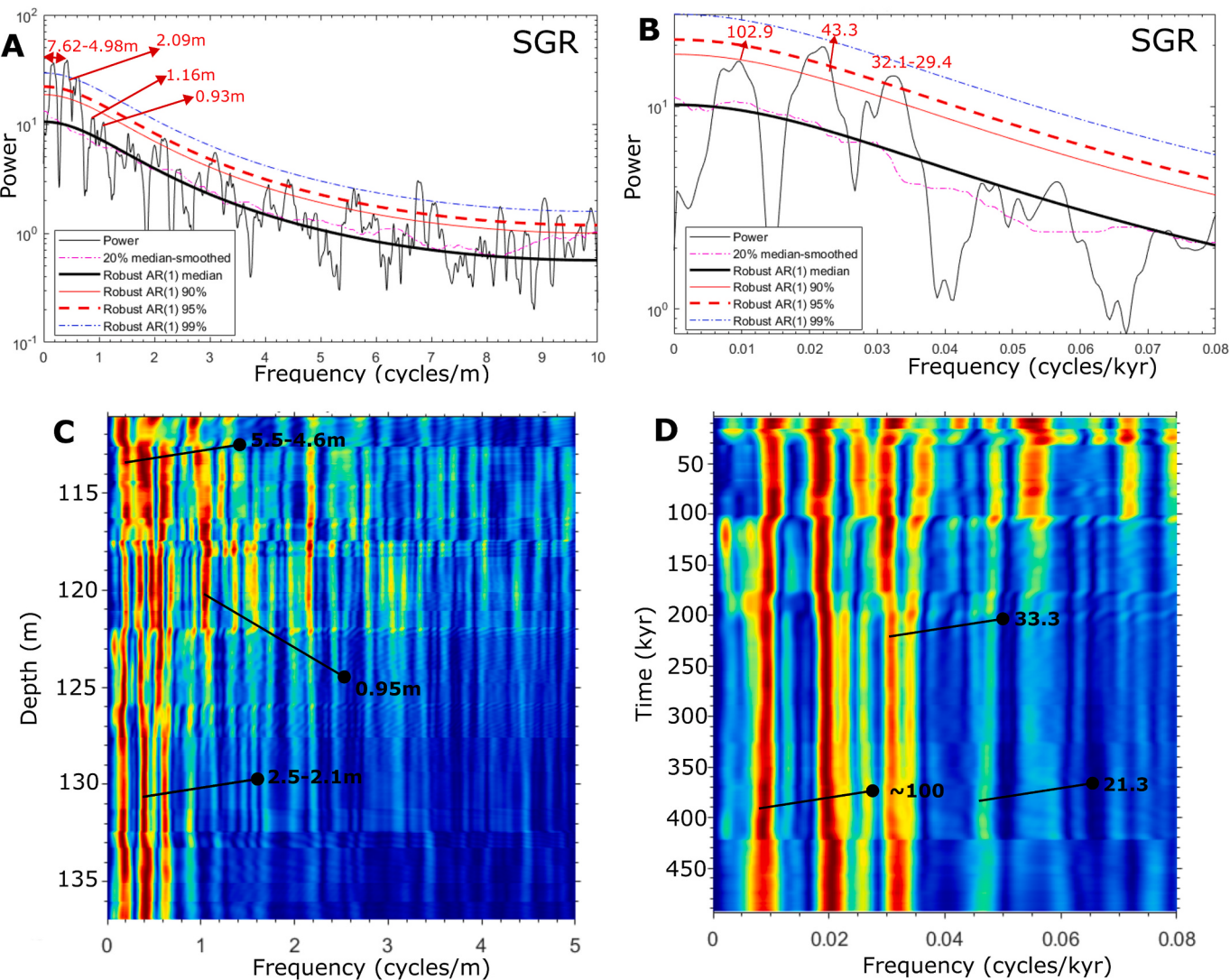


Fig. 9. Spectra and evolutive spectra of the top segment of untuned (A–B) and 100-kyr tuned (C–D) SGR series.

to halokinesis that affected most of Bahrain and eastern Saudi Arabia, which resulted in the so-called Dammam Dome (Edgell, 1996; Weijermars, 1999). Thus, we could expect that the samples are not altered significantly by burial diagenesis (*sensu* Machel, 1997). However, other early diagenetic factors might have occurred to exaggerate the observed carbon excursions (e.g., *syn*-depositional oxidation of organic matter; Patterson and Walter, 1994). Also, the pervasive dolomitization that affected the Khobar member may alter the original signals, albeit Abdullahi et al. (2025) interpreted the dolomite as normal seawater with rock-buffered $\delta^{13}\text{C}$. In sum, the lower half of the formation (strictly before the dolomite interval) could be less altered and more confident to rely on.

5.4. The EECO recognition

As mentioned previously, original stable isotope signatures of shallow marine carbonates can be modified by several diagenetic or secondary processes, including but not restricted to meteoric influx, stabilization of mineral polymorphs (aragonite/HMC to LMC), sulphate reduction, oxidation of organic matter, and burial (Allan and Matthews, 1990; Immenhauser et al., 2002; Swart, 2015). However, numerous workers used whole rock carbonate stable isotope ratios (notably $\delta^{13}\text{C}$), in addition to other proxies, to detect palaeoclimatic changes and events

such as the PETM (e.g., Zamagni et al., 2012; Li et al., 2017) and the Early Eocene hyperthermals (e.g., Kirtland-Turner et al., 2014; Slotnick et al., 2015). Our whole rock $\delta^{13}\text{C}$ shows clear carbon isotope excursions (CIEs) at $\sim 194\text{--}189$ m, $\sim 182\text{--}181$ m, and 168 m (Fig. 11). If we assume the base of the Midra shale member at 52 Ma, based on Weijermars (1999; his Table 1), and use it as the reference bottom point for our ATS, the time range of the first to the last considered excursions will be between 51.75 Ma and 50.2 Ma (which is ~ 15 short eccentricity cycles; Fig. 11). This time interval falls within the EECO event. The carbon excursions observed in this study are also correlated with $\delta^{18}\text{O}$ signals, exhibiting negative excursions at the same depth intervals, a similar trend observed previously by Luciani et al. (2016) for the EECO using bulk sediment carbon and oxygen isotope ratios and by Stap et al. (2010) and Lauretano et al. (2015) for Early Eocene hyperthermals using benthic foraminiferal stable isotope signals. The coherent correlation between the two stable isotopes at the thermal events is interpreted to indicate that the $\delta^{13}\text{C}$ change of the exogenic carbon pool was similarly related to warming during the hyperthermal events (Stap et al., 2010). As was observed previously (e.g., Kirtland-Turner et al., 2014; Luciani et al., 2016), the carbon isotope signal of this study also exhibits a series of CIEs superimposed on background values showing an increasing $\delta^{13}\text{C}$ trend within the EECO interval (Fig. 11). We tentatively interpreted, following Luciani et al. (2016), that as the oxygen isotopes are depleted across the EECO (implying temperature elevation), a general trend of

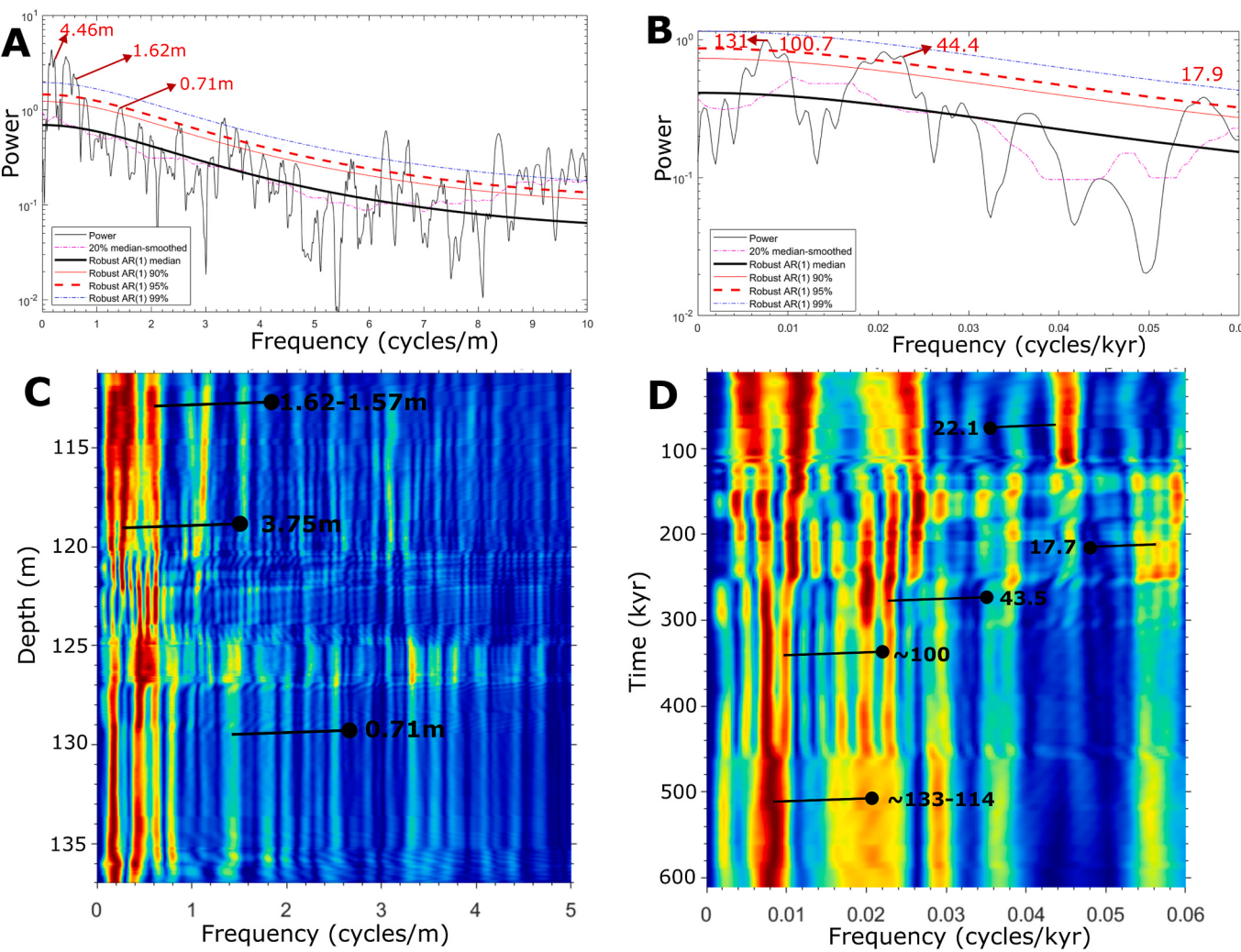


Fig. 10. Spectra and evolutive spectra of the top segment of untuned (A–B) and 100-kyr tuned (C–D) MS series.

carbon isotope increase that is punctuated by negative excursions accompanied it, which may be different when compared with the hyperthermal events (cf. Lauretano et al., 2015).

If we make the same assumption on the age of the base of the Midra shale member as above, the top of the Alveolina Limestone Member is positioned at ~49.7 Ma (~2.3 Myr duration for the ATS), assuming no significant hiatuses are present in this interval. This time interval (52–49.7 Ma) corresponds to a portion of the Eocene Climatic Optimum (EECO), as defined by Zachos et al. (2008), Lauretano et al. (2018), and Filippi et al. (2024)—i.e., ~53 to 49 Ma, or 53.26 to 49.14 Ma as defined by Westerhold et al. (2018, 2020). This suggests that the peak to late stage of the EECO is perhaps represented in the Arabian Dammam Formation by the Midra to Alveolina Limestone members, previously interpreted to have formed in a warm marine environment (Al-Saad, 2005). The warm conditions are further supported by the $\delta^{18}\text{O}$ data (Fig. 11), although some shallow burial resetting cannot be ruled out. The aftermath of the EECO (post-49 Ma) is thus likely represented in the Arabian Dammam Formation by the dolomite- and marly-dominated units of the Khobar Member, deposited during a relatively colder condition, with the dolomite reflecting the transition between warmer and colder conditions (Fig. 11). From ~133 m, $\delta^{13}\text{C}$ abruptly shifted to more negative values that continued into the marl-dominated interval to the top of the core section. This depletion is, however, different from the one observed at the bottom half of the formation in that its depletion shows no clear recovery, and the corresponding $\delta^{18}\text{O}$ signals show a general $\delta^{18}\text{O}$ -enriched trend (unlike the EECO interval). This may explain

cooling with associated oxidation of organic matter, sulphate reduction, or restriction (Zamagni et al., 2012; Swart, 2015).

5.5. Sea level changes

Previous studies have shown that the EECO interval is depleted in $\delta^{18}\text{O}$ values, indicating an increased temperature during the Early Eocene Climatic Event (e.g., Zachos et al., 2001, 2008; Luciani et al., 2016; Westerhold et al., 2018). A similar trend observed in this study could then be used to reason that the bottom half of the formation in this study is warmer, which consequently could suggest higher sea-level conditions, but the climate becomes colder up the formation, especially considering the stable isotope relations above ~133 m. Arguably, the overall trend of the $\delta^{18}\text{O}$ indicates a general increase, suggesting a cooling trend from the bottom to the top of the formation and probably a gradual decrease in sea level. The trend aligns with the view of Al-Saad (2005, his Fig. 5) that the Dammam Formation reflects a long-term regressive sequence and agrees with the depositional environment interpretation of Abdullahi et al. (2025). The coolest part at the top of the formation corresponds to a marl-dominated interval, with relatively higher readings in the SGR log and relatively more positive MS readings (Fig. 2), indicating reduced sea levels that led to less carbonate production and increased detrital flux (Fig. 11). Also, the $\delta^{13}\text{C}$ signal shows an abrupt shift at ~133 m that continued its depletion up the section, and this could be due to a sea-level drop (Zamagni et al., 2012) exaggerated by oxidation of organic matter, sulphate reduction, or

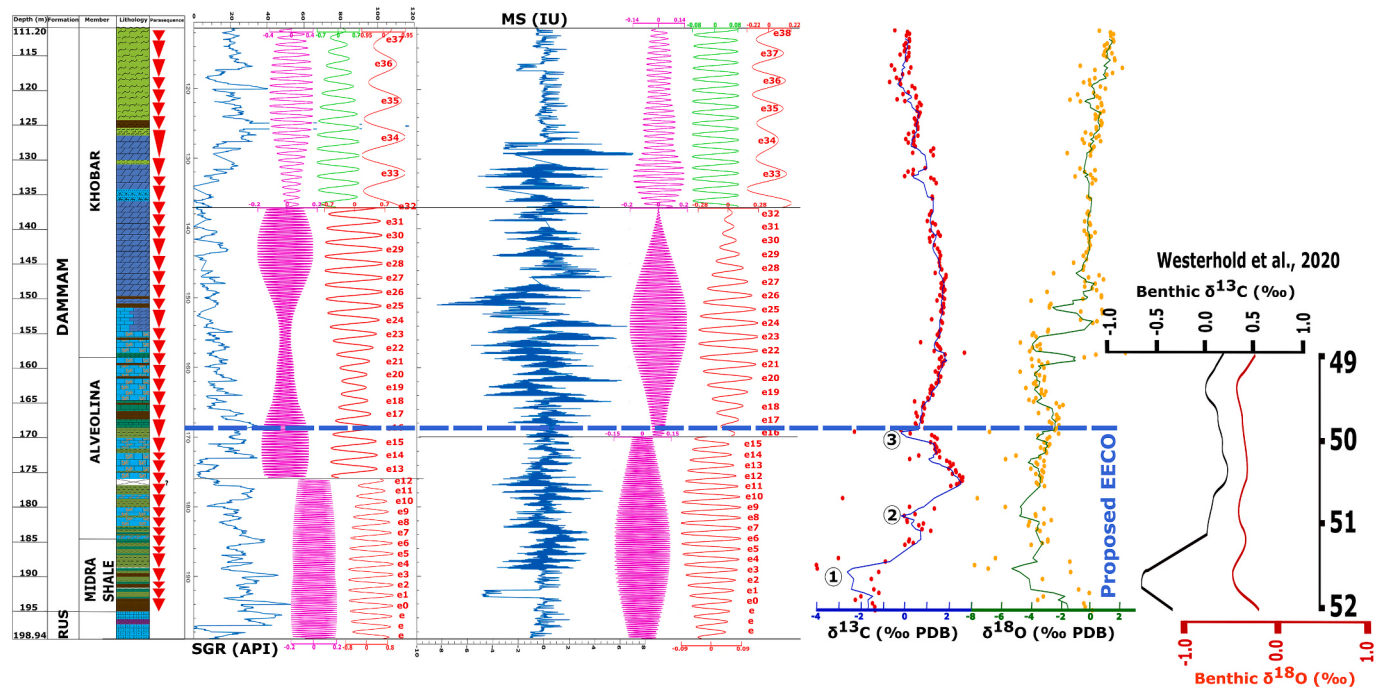


Fig. 11. (First Panel) Stratigraphic log of the analyzed core shown with the identified 5th-order parasequences. (Second and third Panel) Respective SGR and MS logs with 100-kyr (red color) and 20-kyr (pink color) filters of the three segments. 40-kyr filter (green color) is also included on the top segment. The 100-kyr filters are numbered and used for anchoring the basal ATS. Parameters used for filtering the 100-kyr cycles are mentioned in the main text. Those used for the 20-kyr filters are: 3.33 ± 0.002 c/m for the lower segments, 2.5 ± 0.003 c/m for the middle segment, and 1 ± 0.003 c/m and 1.25 ± 0.005 c/m for SGR and MS top segments, respectively. The following are respectively used for filtering the 40-kyr cycles of the SGR and MS top segments: 0.5 ± 0.002 c/m and 0.625 ± 0.005 c/m. (Fourth Panel) Whole rock $\delta^{13}\text{C}$ (blue color) and $\delta^{18}\text{O}$ (green color) plots for the studied Dammam Formation, plotted using 5-point moving average. The proposed EECO excursions are shown on the carbon isotope plot, numbered from 1 to 3. Also shown are the EECO $\delta^{13}\text{C}$ (black color) and $\delta^{18}\text{O}$ (red color) of Westerhold et al. (2020) for the time duration of 52–49 Ma for comparison. (For interpretation of the references to color in this figure legend, the reader is referred to the web version of this article.)

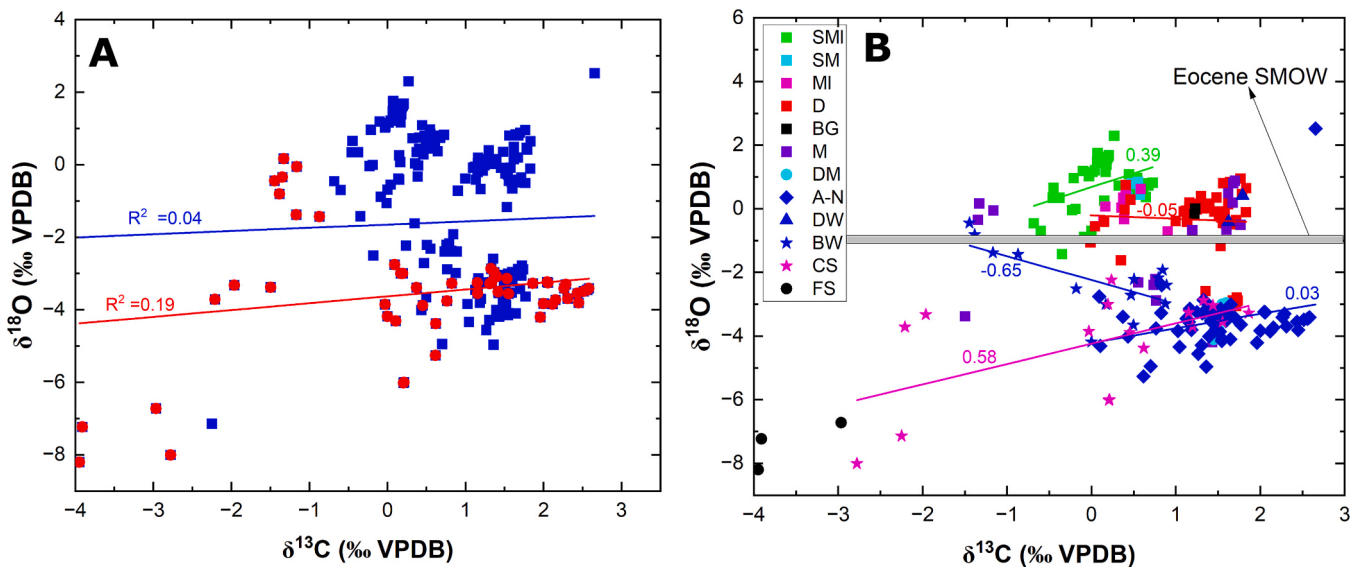


Fig. 12. Whole rock carbonate oxygen and carbon stable isotope cross plots for (A) the whole core section (blue) and the interval between ca. 170 m to the bottom of Dammam Formation (red). The two plots show weak correlations of the stable isotopes, (B) the whole core color-coded by lithofacies. The grey bar represents the estimated Eocene seawater oxygen isotope value of ~ -1 ‰ from Zachos et al. (1994) for comparison. The lithofacies also show dominantly weak correlations. SMI = Shaly marl, SM = Shaly mudstone, MI = Marl, D = Dolomite, BG = Bioclastic grainstone, M = mud, DM = Dolomitic mudstone, DW = Dolomitic wackestone, A-N = Alveolina-Nummulitic limestone, BW = Bioclastic wackestone, CS = Calcareous shale, FS = Fossiliferous shale. (For interpretation of the references to color in this figure legend, the reader is referred to the web version of this article.)

restriction, especially since the interval is interpreted to have been deposited in a relatively restricted setting (Abdullahi et al., 2025).

Minor cyclical regressions and transgressions in the Dammam Formation, reflecting short-term changes, have been noted by Al-Saad (2005), Holail et al. (2005), and Khalaf et al. (2018), as well as in the cyclic parasequences observed here. The short eccentricity-pacing of the parasequence, especially within the lower and middle segments of the formation, suggests astronomical forcing of both the ambient climate and sea-level changes. Al-Saad (2005) suggested that the Dammam Formation was predominantly formed in a warm shallow marine environment, mainly due to extensive dolomitization and the presence of *Alveolines*, *Linderines*, and *Nummulites*. The stable isotope data from this study also shows lower values in the section corresponding to the thick cyclic *Alveolina-Nummulitic* limestones (typical of Eocene marine calcite that precipitated at temperatures of 25–35 °C), further supporting the idea of a warm shallow marine environment. Interestingly, eCOCO (Fig. 4) indicates that this *Alveolina-Nummulitic* interval has a relatively higher sedimentation rate compared to the interval underlying it. This could imply that the warming trend increased relative sea-level, which, coupled with the less turbid conditions (Weijermars, 1999) favored the *Alveolina-Nummulitic* factory, resulting in the deposition of this interval at a relatively faster sedimentation rate, as also documented in middle Eocene carbonate systems around the Tethyan realm (Messaoud et al., 2023; Morabito et al., 2024).

5.6. Astronomical forcing and Eocene palaeoclimate

Figs. 2, 3, and 11 show the identified parasequences and how they vertically changed through the studied stratigraphic interval. The bottommost half is dominated by lithological cycles that are based by fossiliferous shales and mudstones and capped by bioclastic wackestones. This changes to cyclic basal calcareous shales and organic-rich mudstones that are capped by *Alveolina*-rich wacke-packstones, *Nummulitic*-rich wacke-packstones, or *Alveolina-Nummulitic* wacke-packstones. These cycles often exhibit higher SGR and MS values at their base but lower at their top. Filtering of the respective SGR and MS series indicates that these shoaling upward parasequences are dominantly paced by short eccentricity, supporting the hypothesis that they are likely astronomically forced. The eccentricity-pacing of these stratigraphic cycles agrees well with other cyclostratigraphic studies of Eocene Series (e.g., Lauretano et al., 2015, 2018; Messaoud et al., 2023; Brachert et al., 2023). Additionally, the COCO optimal sedimentation rates show a null hypothesis significance level of <1% (Fig. 4), supporting the acceptance of astronomical forcing on the deposition of the Dammam Formation and rejection of the null hypothesis of no astronomical forcing (Li et al., 2018, 2019). The presence of both low- and high-frequency cycles (Figs. 5–10) and the close match between some of the stratigraphic power cycles of the Dammam Formation and the target cycles of Laskar et al. (2004) are also supportive of Milankovitch forcing.

Generally, low SGR and MS readings are recorded for the Eocene Dammam Formation. These low values could be due to the overall hot-warmhouse condition during the Early-Middle Eocene time (Pearson et al., 2007; Westerhold et al., 2020) that was amplified by the PETM, the EECO, and other minor warming reversals or hyperthermals. In the tropical Arabian Peninsula, this resulted in the deposition of shallow marine carbonates with low magnetic and radioactive content.

5.7. Age uncertainty and astronomical time scale

As highlighted above, different ages have been assigned to the Dammam Formation. Although Weijermars' (1999) study was on outcrops, because the core utilized in this study was extracted from nearly the same locality as Weijermars' (Dammam Dome and KFUPM localities vs. KFUPM Beach locality; both localities are in Khobar, Eastern Saudi Arabia, with the latter being ~6 km to the south of the former), we assumed a similar age and duration for the Dammam Formation here,

that is, a duration of 8.2 Myr (52–43.8 Ma). The floating astronomical time scale (ATS), constructed by 100 kyr-minimal tuning of both the SGR and MS data series based on optimal SARs of each segment, amounted to a total duration of ~4 Myr. The duration discrepancies could be explained by many reasons including (i) the absence of the topmost member of the formation, Alat Member, at the KFUPM Beach location; (ii) the possibility of hiatuses within the studied interval, which cannot be accounted for by the approach employed in this study; and (iii) the age uncertainty of the considered independent age constraints could also be another source of the disparity between the two durations. This study therefore needs further investigation through absolute age dating of the studied core or similar stratigraphic interval.

6. Conclusion

This study used coupled continuous core-based SGR and MS data obtained from a shallow subsurface core of the Lower-Middle Eocene Dammam Formation to unravel the sedimentation rate and the possibility of astronomical forcing on the stratigraphic sequence. The sedimentation rates are relatively low and range from ~1.5 to 5 cm/kyr. The fine-carbonate-dominated Midra Member recorded a stable sedimentation rate, indicating settling of fines during Ypresian turbid marine conditions as transgression of the Arabian plate began.

Based on the stable isotope results, this study indicates that the formation represents an overall shallow warm marine environment that shows progressive cooling from its bottom to top units with intermittent reversals. Thus, as suggested previously, we concluded that the formation represents a long-term regressive cycle with intermittent short-term cycles represented by the meter-scale shallowing-upward parasequences that were astronomically forced. The EECO period is likely represented in the Arabian Plate by the shales and *Alveolina-Nummulitic* units of the Midra and *Alveolina* Limestone members of the Dammam Formation whereas dolomites and marly-dominated units of the Khobar Member represent the aftermath of the optimum.

The study confirmed Milankovitch forcing on deposition of the Dammam Formation with short eccentricity (125 kyr, ~100 kyr), obliquity (40 kyr), and precession (20 kyr) cycles evident. Eccentricity was the dominant force, similar to that reported for other Tethyan and global Eocene Series. A duration of ~4 Myr was recorded for the shallow core of the Dammam Formation in this locality, which is attributed to the non-deposition of the topmost member of the formation, and the probable presence of hiatuses. This study provides the first assessment of Milankovitch forcing during and after the EECO marine records of the Arabian Plate, which can be compared regionally, especially since the formation is regionally correlative, and with other global records of the event.

CRediT authorship contribution statement

Misbahu Abdullahi: Writing – review & editing, Writing – original draft, Visualization, Software, Investigation, Formal analysis, Data curation. **Taimur Khan:** Writing – review & editing, Writing – original draft, Visualization, Formal analysis, Data curation. **Samer Aljurf:** Writing – original draft, Formal analysis, Data curation. **Vagif Suleymanov:** Writing – review & editing, Methodology, Formal analysis, Data curation. **Adhipa Herlambang:** Writing – review & editing, Methodology, Formal analysis, Data curation. **Michele Morsilli:** Writing – review & editing, Supervision. **Khalid Al-Ramadan:** Writing – review & editing. **Ardiansyah Koeshidayatullah:** Writing – review & editing, Writing – original draft, Validation, Supervision, Investigation, Funding acquisition, Conceptualization.

Declaration of competing interest

The authors declare the following financial interests/personal relationships which may be considered as potential competing interests:

Ardiansyah Koeshidayatullah reports financial support was provided by KFUPM. If there are other authors, they declare that they have no known competing financial interests or personal relationships that could have appeared to influence the work reported in this paper.

Acknowledgements

The authors would like to thank the Geosciences Department of the College of Petroleum Engineering and Geosciences, King Fahd University of Petroleum and Minerals, for access to the laboratory and startup project SF21011. We would like to also thank the CPG Learning Enrichment Center Initiative, in particular Dr Ammar ElHusseiny for providing access to the cores. We also appreciate the constructive feedback provided by the late Prof. Fred Read, the editors and two anonymous reviewers on the earlier version of the manuscript, which has significantly improved its quality.

Appendix A. Supplementary data

Supplementary data to this article can be found online at <https://doi.org/10.1016/j.palaeo.2025.113298>.

Data availability

All data used in this study is available in the supplementary material.

References

- Abdullahi, M., Herlambang, A., Al-Ramadan, K., Koeshidayatullah, A., 2025. Mechanisms of near-normal sea water dolomitisation: Mesohaline-reflux or syn-depositional? *The Depo Rec.* 00, 1–23. <https://doi.org/10.1002/dep2.70039>.
- Adabi, M.H., Zohdi, A., Ghabeishavi, A., Amiri-Bakhtiyar, H., 2008. Applications of nummulitids and other larger benthic foraminifera in depositional environment and sequence stratigraphy: an example from the Eocene deposits in Zagros Basin, SW Iran. *Facies* 54, 499–512. <https://doi.org/10.1007/s10347-008-0151-7>.
- Al-Fares, A.A., Bouman, M., Jeans, P., 1998. A new look at the Middle to lower cretaceous stratigraphy, offshore Kuwait. *GeoArab* 3, 543–560. <https://doi.org/10.2113/geoarabia0304543>.
- Al-Hashimi, H.A., Amer, R.M., 1985. Tertiary microfacies of Iraq. *Dir. Gen. Geol. Surv. Min. Invest.* 56.
- Allan, J.R., Matthews, R.K., 1990. Isotope signatures associated with early meteoric diagenesis. *Carb. Dia.* 197–217. <https://doi.org/10.1002/9781444304510.ch16>.
- Al-Saad, H., 2005. Lithostratigraphy of the middle Eocene Dammann Formation in Qatar, Arabian Gulf: effects of sea-level fluctuations along a tidal environment. *J. Asian Earth Sci.* 25, 781–789. <https://doi.org/10.1016/j.jseas.2004.07.009>.
- Asquith, G.B., Krygowski, D., 2004. Basic Well Log Analysis, 2nd ed. Am. Ass. Petr. Geo. Tulsa, Oklahoma, pp. 305–371.
- Banerjee, S., Khanolkar, S., Saraswati, P.K., 2018. Facies and depositional settings of the middle Eocene-Oligocene carbonates in Kutch. *Geodin. Acta* 30, 119–136. <https://doi.org/10.1080/09853111.2018.1442609>.
- Barrera, E., Huber, B.T., Kennett, J.P., Warnke, D.A., 1993. Eocene to Oligocene oceanography and temperatures in the Antarctic Indian Ocean. The Antarctic paleoenvironment: a perspective on global change. *Am. Geophys. Uni. Ant. Res. Ser.* 60, 49–65. <https://doi.org/10.1002/9781118668061.ch3>.
- Bohaty, S.M., Zachos, J.C., 2003. Significant southern ocean warming event in the late middle Eocene. *Geology* 31, 1017–1020. <https://doi.org/10.1130/G19800.1>.
- Boulila, S., Galbrun, B., Hinnov, L.A., Collin, P.Y., 2008. High-resolution cyclostratigraphic analysis from magnetic susceptibility in a lower Kimmeridgian (Upper Jurassic) marl-limestone succession (La Méouge, Vercors Basin, France). *Sediment. Geol.* 203, 54–63. <https://doi.org/10.1016/j.sedgeo.2007.10.004>.
- Bowen, G.J., Beerling, D.J., Koch, P.L., Zachos, J.C., Quattlebaum, T., 2004. A humid climate state during the Palaeocene/Eocene thermal maximum. *Nature* 432, 495–499. <https://doi.org/10.1038/nature03115>.
- Brachert, T.C., Agnini, C., Gagnon, C., Gély, J.P., Henehan, M.J., Westerhold, T., 2023. Astronomical pacing of middle Eocene Sea-level fluctuations: Inferences from shallow-water carbonate ramp deposits. *Paleoceanogr. Paleoclimatol.* 38, e2023PA004633. <https://doi.org/10.1029/2023PA004633>.
- Budd, D.A., Hiat, E.E., 1993. Mineralogical stabilization of high-magnesium calcite; geochemical evidence for intracrystalline recrystallization within Holocene porcellaneous foraminifera. *J. Sediment. Res.* 63, 261–274. <https://doi.org/10.1306/D4267AD7-2B26-11D7-8648000102C1865D>.
- Chen, T., Xu, H., Lu, A., Xu, X., Peng, S., Yue, S., 2004. Direct evidence of transformation from smectite to palygorskite: TEM investigation. *Sci. China Series D Earth Sci.* 47, 985–994.
- Cramwinckel, M.J., Huber, M., Kocken, I.J., Agnini, C., Bijl, P.K., Bohaty, S.M., Frielings, J., Goldner, A., Hilgen, F.J., Kip, E.L., Peterse, F., 2018. Synchronous tropical and polar temperature evolution in the Eocene. *Nature* 559, 382–386. <https://doi.org/10.1038/s41586-018-0272-2>.
- Dickens, G.R., O’Neil, J.R., Rea, D.K., Owen, R.M., 1995. Dissociation of oceanic methane hydrate as a cause of the carbon isotope excursion at the end of the Paleocene. *Paleoceanography* 10, 965–971. <https://doi.org/10.1029/95PA02087>.
- Edgett, H.S., 1996. Salt tectonism in the Persian Gulf basin. *Geol. Soc. Lond. Spec. Pub.* 100, 129–151. <https://doi.org/10.1144/GSL.SP.1996.100.01.10>.
- Ellwood, B.B., Crick, R.E., El Hassani, A., 1999. The magnetotusceptibility event and cyclostratigraphy (MSEC) method used in geological correlation of Devonian rocks from Anti-Atlas Morocco. *AAPG Bull.* 83, 1119–1134. <https://doi.org/10.1306/E4FD2E8D-1732-11D7-8645000102C1865D>.
- Ellwood, B.B., Crick, R.E., Hassani, A.E., Benoit, S.L., Young, R.H., 2000. Magnetotusceptibility event and cyclostratigraphy method applied to marine rocks: detrital input versus carbonate productivity. *Geology* 28, 1135–1138. [https://doi.org/10.1130/0091-7613\(2000\)28<1135:MEACMA>2.0.CO;2](https://doi.org/10.1130/0091-7613(2000)28<1135:MEACMA>2.0.CO;2).
- Evans, D., Sagoo, N., Renema, W., Cotton, L.J., Müller, W., Todd, J.A., Saraswati, P.K., Stassen, P., Ziegler, M., Pearson, P.N., Valdes, P.J., 2018. Eocene greenhouse climate revealed by coupled clumped isotope-Mg/ca thermometry. *Proc. Natl. Acad. Sci.* 115, 1174–1179. <https://doi.org/10.1073/pnas.1714744115>.
- Filippi, G., Barrett, R., Schmidt, D.N., D’Onofrio, R., Westerhold, T., Brombin, V., Luciani, V., 2024. Impacts of the early Eocene Climatic Optimum (EECO, ~53–49 Ma) on planktic foraminiferal resilience. *Paleoceanogr. Paleoclimatol.* 39, e2023PA004820. <https://doi.org/10.1029/2023PA004820>.
- Giorgioni, M., Jovane, L., Rego, E.S., Rodelli, D., Frontalini, F., Coccioni, R., Catanzariti, R., Özcan, E., 2019. Carbon cycle instability and orbital forcing during the Middle Eocene Climatic Optimum. *Sci. Rep.* 9, 9357. <https://doi.org/10.1038/s41598-019-45763-2>.
- Hammer, Ø., Harper, D.A., Ryan, P., 2001. Past: paleontological statistics software package for education and data analysis. *Palaeontol. Electron.* 4, 1. http://palaeo-electronica.org/2001_1/past/issue1_01.htm.
- Hassan, M., Hossin, A., Combaz, A., 1976. Fundamentals of the differential gamma ray log-interpretation technique. In: SPWLA Ann. Logg. Sympos.
- Hinnov, L.A., 2018. Cyclostratigraphy and astrochronology in 2018. *Stratigr. Timesc.* 3, 1–80. <https://doi.org/10.1016/bs.strats.2018.08.004>.
- Holail, H.M., Shaaban, M.N., Mansour, A.S., Rifai, R.I., 2005. Diagenesis of the middle Eocene upper Damman subformation, Qatar. Petrographic and isotopic evidence. *Carbonates Evaporites* 20, 72–81. <https://doi.org/10.1007/BF03175450>.
- Huang, C., Hinnov, L., 2019. Astronomically forced climate evolution in a saline lake record of the middle Eocene to Oligocene, Jianghan Basin, China. *Earth Planet. Sci. Lett.* 528, 115846. <https://doi.org/10.1016/j.epsl.2019.115846>.
- Immenhauser, A., Kenter, J.A., Ganssen, G., Bahamonde, J.R., Van Vliet, A., Saher, M.H., 2002. Origin and significance of isotope shifts in Pennsylvanian carbonates (Asturias, NW Spain). *J. Sediment. Res.* 72, 82–94. <https://doi.org/10.1306/051701720082>.
- Kennett, J.P., Stott, L.D., 1991. Abrupt deep-sea warming, palaeoceanographic changes and benthic extinctions at the end of the Palaeocene. *Nature* 353, 225–229. <https://doi.org/10.1038/353225a0>.
- Khalaif, F.I., Abdullah, F.A., Gharib, I.M., 2018. Petrography, diagenesis and isotope geochemistry of dolostones and dolocretes in the Eocene Damman Formation, Kuwait, Arabian Gulf. *Carbonates Evaporites* 33, 87–105. <https://doi.org/10.1007/s13146-016-0330-5>.
- Kim, S.T., O’Neil, J.R., 1997. Equilibrium and nonequilibrium oxygen isotope effects in synthetic carbonates. *Geochim. Cosmochim. Acta* 61, 3461–3475. [https://doi.org/10.1016/S0016-7037\(97\)00169-5](https://doi.org/10.1016/S0016-7037(97)00169-5).
- Kirtland-Turner, S., Sexton, P.F., Charles, C.D., Norris, R.D., 2014. Persistence of carbon release events through the peak of early Eocene global warmth. *Nat. Geosci.* 7, 748–751. <https://doi.org/10.1038/ngeo2240>.
- Kodama, K.P., Hinnov, L., 2015. Rock Magnetic Cyclostratigraphy. Wiley-Blackwell.
- Kurtz, A.C., Kump, L.R., Arthur, M.A., Zachos, J.C., Paytan, A., 2003. Early Cenozoic decoupling of the global carbon and sulfur cycles. *Paleoceanography* 18 (4). <https://doi.org/10.1029/2003PA000908>.
- Land, L.S., 1980. The Isotopic and Trace Element Geochemistry of Dolomite: The State of the Art. SEPM Spec. Publ., Tulsa, Oklahoma, USA, pp. 87–110. <https://doi.org/10.2110/pec.80.28.0087>.
- Laskar, J., Robutel, P., Joutel, F., Gastineau, M., Correia, A.C.M., Levrard, B., 2004. A long-term numerical solution for the insolation quantities of the Earth. *Astron. Astrophys.* 428, 261–285. <https://doi.org/10.1051/0004-6361:20041335>.
- Lauretano, V., Little, K., Polling, M., Zachos, J.C., Lourens, L.J., 2015. Frequency, magnitude and character of hyperthermal events at the onset of the early Eocene Climatic Optimum. *Clim. Past* 11, 1313–1324. <https://doi.org/10.5194/cp-11-1313-2015>.
- Lauretano, V., Zachos, J.C., Lourens, L.J., 2018. Orbitally paced carbon and deep-sea temperature changes at the peak of the early Eocene Climatic Optimum. *Paleoceanogr. Paleoclimatol.* 33, 1050–1065. <https://doi.org/10.1029/2018PA003422>.
- Li, J., Hu, X., Garzanti, E., BouDagher-Fadel, M., 2017. Shallow-water carbonate responses to the Paleocene-Eocene thermal maximum in the Tethyan Himalaya (southern Tibet): Tectonic and climatic implications. *Palaeogeogr. Palaeoclimatol. Palaeoecol.* 466, 153–165. <https://doi.org/10.1016/j.palaeo.2016.11.026>.
- Li, M., Kump, L.R., Hinnov, L.A., Mann, M.E., 2018. Tracking variable sedimentation rates and astronomical forcing in Phanerozoic paleoclimate proxy series with evolutionary correlation coefficients and hypothesis testing. *Earth Planet. Sci. Lett.* 501, 165–179. <https://doi.org/10.1016/j.epsl.2018.08.041>.
- Li, M., Hinnov, L., Kump, L., 2019. Acycle: Time-series analysis software for paleoclimate research and education. *Comput. Geosci.* 127, 12–22. <https://doi.org/10.1016/j.cageo.2019.02.011>.

- Luciani, V., Dickens, G.R., Backman, J., Fornaciari, E., Giusberti, L., Agnini, C., D'Onofrio, R., 2016. Major perturbations in the global carbon cycle and photosymbiont-bearing planktic foraminifera during the early Eocene. *Clim. Past* 12, 981–1007. <https://doi.org/10.5194/cp-12-981-2016>.
- Machel, H.G., 1997. Recrystallization versus neomorphism, and the concept of 'significant recrystallization' in dolomite research. *Sediment. Geol.* 113, 161–168. [https://doi.org/10.1016/S0037-0738\(97\)00078-X](https://doi.org/10.1016/S0037-0738(97)00078-X).
- Mann, M.E., Lees, J.M., 1996. Robust estimation of background noise and signal detection in climatic time series. *Clim. Chang.* 33, 409–445. <https://doi.org/10.1007/BF00142586>.
- Martín-Martín, M., Tosquella, J., Guerrera, F., Maaté, A., Martín-Algarra, A., 2025. The Eocene carbonate platforms of the westernmost Tethys: a review. *Int. Geol. Rev.* 67, 573–605. <https://doi.org/10.1080/00206814.2024.2397804>.
- Messaoud, J.H., Thibault, N., De Vleeschouwer, D., Monkenbusch, J., 2023. Benthic biota (nummulites) response to a hyperthermal event: Eccentricity-modulated precession control on climate during the middle Eocene warming in the Southern Mediterranean. *Palaeogeogr. Palaeoclimatol. Palaeoecol.* 626, 111712. <https://doi.org/10.1016/j.palaeo.2023.111712>.
- Morabito, C., Papazzoni, C.A., Lehrmann, D.J., Payne, J.L., Al-Ramadan, K., Morsilli, M., 2024. Carbonate factory response through the MECO (Middle Eocene climate Optimum) event: Insight from the Apulia Carbonate Platform, Gargano Promontory, Italy. *Sed. Geol.* 461, 106575. <https://doi.org/10.1016/j.sedgeo.2023.106575>.
- Paillard, D., Labeyrie, L., Yiou, P., 1996. Macintosh program performs time-series analysis. *EOS Trans. Am. Geophys. Union* 77, 379. <https://doi.org/10.1029/96EO00259>.
- Patterson, W.P., Walter, L.M., 1994. Syndepositional diagenesis of modern platform carbonates: evidence from isotopic and minor element data. *Geology* 22, 127–130. [https://doi.org/10.1130/0091-7613\(1994\)022%3C0127:SDOMPC%3E2.3.CO;2](https://doi.org/10.1130/0091-7613(1994)022%3C0127:SDOMPC%3E2.3.CO;2).
- Pearson, P.N., van Dongen, B.E., Nicholas, C.J., Pancost, R.D., Schouten, S., Singano, J. M., Wade, B.S., 2007. Stable warm tropical climate through the Eocene epoch. *Geology* 35, 211–214. <https://doi.org/10.1130/G23175A.1>.
- Peng, C., Zou, C., Zhang, S., Shu, J., Wang, C., 2024. Geophysical logs as proxies for cyclostratigraphy: Sensitivity evaluation, proxy selection, and paleoclimatic interpretation. *Earth Sci. Rev.* 252, 104735. <https://doi.org/10.1016/j.earscirev.2024.104735>.
- Powers, R., Ramirez, L.F., Redmond, C., Elberg Jr., E., 1966. Geology of the Arabian Peninsula: Sedimentary Geology of Saudi Arabia. Technical Report. US Geol. Surv.
- Sharland, P., Archer, R., Casey, D., Davies, R., Hall, S., Heward, A., Horbury, A., Simmons, M., 2001. Arabian Plate Sequence Stratigraphy. *GeoArab. Spec. Pub.*
- Slotnick, B.S., Dickens, G.R., Hollis, C.J., Crampton, J.S., Percy Strong, C., Phillips, A., 2015. The onset of the early Eocene climatic optimum at branch stream, Clarence River valley, New Zealand. *New Zeal. J. Geol. Geophys.* 58, 262–280. <https://doi.org/10.1080/00288306.2015.1063514>.
- Stap, L., Lourens, L.J., Thomas, E., Sluijs, A., Bohaty, S., Zachos, J.C., 2010. High-resolution deep-sea carbon and oxygen isotope records of Eocene thermal Maximum 2 and H2. *Geology* 38, 607–610. <https://doi.org/10.1130/G30777.1>.
- Swart, P.K., 2015. The geochemistry of carbonate diagenesis: the past, present and future. *Sedimentology* 62, 1233–1304. <https://doi.org/10.1111/sed.12205>.
- Tarutani, T., Clayton, R.N., Mayeda, T.K., 1969. The effect of polymorphism and magnesium substitution on oxygen isotope fractionation between calcium carbonate and water. *Geochim. Cosmochim. Acta* 33, 987–996. [https://doi.org/10.1016/0016-7037\(69\)90108-2](https://doi.org/10.1016/0016-7037(69)90108-2).
- Teele, J.W., 1973. Surface geology of Dammam dome, eastern province, Saudi Arabia. *AAPG Bull.* 57, 558–576. <https://doi.org/10.1306/819A4304-16C5-11D7-8645000102C1865D>.
- Wahl, J.S., 1983. Gamma-ray logging. *Geophysics* 48, 1536–1550. <https://doi.org/10.1190/1.1441436>.
- Weaver, C.E., Beck, K.C., 1977. Miocene of the SE United States: a model for chemical sedimentation in a peri-marine environment. *Sediment. Geol.* 17, IX–234. [https://doi.org/10.1016/0037-0738\(77\)90062-8](https://doi.org/10.1016/0037-0738(77)90062-8).
- Weedon, G.P., 2022. Problems with the current practice of spectral analysis in cyclostratigraphy: avoiding false detection of regular cyclicity. *Earth Sci. Rev.* 235, 104261. <https://doi.org/10.1016/j.earscirev.2022.104261>.
- Weijermars, R., 1999. Surface geology, lithostratigraphy and tertiary growth of the Dammam dome, Saudi Arabia: a new field guide. *GeoArab* 4, 199–226. <https://doi.org/10.2113/geoarabia0402199>.
- Westerhold, T., Röhl, U., 2009. High resolution cyclostratigraphy of the early Eocene—new insights into the origin of the Cenozoic cooling trend. *Clim. Past* 5, 309–327. <https://doi.org/10.5194/cp-5-309-2009>.
- Westerhold, T., Röhl, U., Donner, B., Zachos, J.C., 2018. Global extent of early Eocene Hyperthermal events: a new Pacific benthic foraminiferal isotope record from Shatsky rise (ODP Site 1209). *Paleoceanogr. Paleoceanol.* 33, 626–642. <https://doi.org/10.1029/2017PA003306>.
- Westerhold, T., Marwan, N., Drury, A.J., Liebrand, D., Agnini, C., Anagnostou, E., Barnet, J.S., Bohaty, S.M., De Vleeschouwer, D., Florindo, F., Frederichs, T., Hodell, D.A., Holburn, A.E., Kroon, D., Lauretano, V., Littler, K., Lourens, L.J., Lyle, M., Pälike, H., Röhl, U., Tian, J., Wilkens, R.H., Wilson, P.A., Zachos, J.C., 2020. An astronomically dated record of Earth's climate and its predictability over the last 66 million years. *Science* 369, 1383–1387. <https://doi.org/10.1126/science.aba6853>.
- Wu, S.Y., Liu, J., Chen, J.W., Wu, H.R., 2021. Characteristics of Milankovitch cycles recorded in Eocene strata in the eastern depression of North Yellow Sea Basin, North China. *China Geol.* 4, 274–287. <https://doi.org/10.31035/cg2021002>.
- Wu, H., Fang, Q., Hinnoo, L.A., Zhang, S., Yang, T., Shi, M., Li, H., 2023. Astronomical time scale for the Paleozoic Era. *Earth Sci. Rev.* 244, 104510. <https://doi.org/10.1016/j.earscirev.2023.104510>.
- Xie, Q., Chen, T., Zhou, H., Xu, X., Xu, H., Ji, J., Lu, H., Balsam, W., 2013. Mechanism of palygorskite formation in the Red Clay Formation on the Chinese Loess Plateau, Northwest China. *Geoderma* 192, 39–49. <https://doi.org/10.1016/j.geoderma.2012.07.021>.
- Zachos, J.C., Lohmann, K.C., Walker, J.C., Wise, S.W., 1993. Abrupt climate change and transient climates during the Paleogene: a marine perspective. *J. Geol.* 101, 191–213. <https://doi.org/10.1086/648216>.
- Zachos, J.C., Stott, L.D., Lohmann, K.C., 1994. Evolution of early Cenozoic marine temperatures. *Paleoceanography* 9, 353–387. <https://doi.org/10.1029/93PA03266>.
- Zachos, J., Pagani, M., Sloan, L., Thomas, E., Billups, K., 2001. Trends, rhythms, and aberrations in global climate 65 Ma to present. *Science* 292, 686–693. <https://doi.org/10.1126/science.1059412>.
- Zachos, J.C., Bohaty, S., Quattlebaum, T., Sluijs, A., Brinkhuis, H., Gibbs, S. J., Bralower, T.J., 2006. Extreme warming of mid-latitude coastal ocean during the Paleocene-Eocene thermal Maximum: Inferences from TEX86 and isotope data. *Geology* 34, 737–740. <https://doi.org/10.1130/G22522.1>.
- Zachos, J.C., Dickens, G.R., Zeebe, R.E., 2008. An early Cenozoic perspective on greenhouse warming and carbon-cycle dynamics. *Nature* 451, 279–283. <https://doi.org/10.1038/nature06588>.
- Zamagni, J., Mutti, M., Ballato, P., Košir, A., 2012. The Paleocene–Eocene thermal maximum (PETM) in shallow-marine successions of the Adriatic carbonate platform (SW Slovenia). *GSA Bull.* 124, 1071–1086. <https://doi.org/10.1130/B30553.1>.
- Zeebe, R.E., Zachos, J.C., 2013. Long-term legacy of massive carbon input to the Earth system: Anthropocene versus Eocene. *Philos. Trans. Roy. Soc. A Math. Phys. Eng. Sci.* 371, 20120006. <https://doi.org/10.1098/rsta.2012.0006>.
- Ziegler, M.A., 2001. Late Permian to Holocene paleofacies evolution of the Arabian Plate and its hydrocarbon occurrences. *GeoArab* 6, 445–504. <https://doi.org/10.2113/geoarabia0603445>.